Pan-ErbB inhibition protects from SARS-CoV-2 replication, inflammation, and injury

Sirle Saul [1, 12], Marwah Karim[1, 12], Pei Tzu Huang[1, 13], Luca Ghita[1,13], Winston Chiu[2], Sathish Kumar[1], Nishank Bhalla[3], Pieter Leyssen[2], Courtney Cohen[4], Kathleen Huie[4], Courtney Tindle[5, 6], Malaya Sahoo[7], Mamdouh Sibai [7], Benjamin A. Pinsky[7, 1], Soumita Das[6, 8], Pradipta Ghosh[5, 6, 9], John Dye[4], David Solow-Cordero[10], Jing Jin[11], Dirk Jochmans [2], Johan Neyts[2], Aarthi Narayanan[3], Steven De Jonghe[2], and Shirit Einav[1, *]

[1]Department of Medicine, Division of Infectious Diseases and Geographic Medicine, and Department of Microbiology and Immunology, Stanford University, CA, USA
[2] KU Leuven, Department of Microbiology, Immunology and Transplantation, Rega Institute for Medical Research, Laboratory of Virology and Chemotherapy, Belgium
[3]National Center for Biodefence and Infectious Disease, Biomedical Research Laboratory, School of Systems Biology, George Mason University, Manassas, VA, USA.
[4]US Army Medical Research Institute of Infectious Diseases, Viral Immunology Branch, Fort Detrick, Maryland
[5] Department of Cellular and Molecular Medicine, University of California San Diego
[6] HUMANOID CoRE, University of California San Diego.
[7]Department of Pathology, Stanford University School of Medicine, Stanford, California, USA
[8]Department of Pathology, University of California San Diego
[9]Department of Medicine, University of California San Diego
[10]High-Throughput Bioscience Center, Department of Chemical and Systems Biology, Stanford University, CA
[11] Vitalant Research Institute, San Francisco, CA, USA

* Corresponding author and lead contact: seinav@stanford.edu

[12]These authors contributed equally
[13]These authors also contributed equally

Summary

Effective therapies are needed to combat emerging viruses. Seventeen candidates that rescue cells from SARS-CoV-2-induced lethality and target diverse functions emerged in a screen of 4,413 compounds. Among the hits was lapatinib, an approved inhibitor of the ErbB family of receptor tyrosine kinases. Lapatinib and other pan-ErbB inhibitors suppress replication of SARS-CoV-2 and unrelated viruses with a high barrier to resistance. ErbB4, but not lapatinib's cancer targets ErbB1 and ErbB2, is required for SARS-CoV-2 entry and Venezuelan equine encephalitis virus infection and is a molecular target mediating lapatinib's antiviral effect. In human lung organoids, lapatinib protects from SARS-CoV-2-induced activation of pathways implicated in acute and chronic lung injury downstream of ErbBs (p38-MAPK, MEK/ERK, and AKT/mTOR), pro-inflammatory cytokine production, and epithelial barrier injury. These findings reveal regulation of viral infection, inflammation, and tissue injury via ErbBs and propose approved candidates to counteract these effects with implications for coronaviruses and unrelated viruses.

Key words

SARS-CoV-2 infection, emerging viruses, ErbB, kinase inhibitors, high-throughput screen, broad-spectrum antivirals, drug repurposing, inflammation, lung injury

Introduction

The recently emerging severe acute respiratory syndrome coronavirus-2 (SARS-CoV-2) has spread globally, resulting in the Coronavirus Disease 2019 (COVID-19) pandemic. While most infected individuals remain asymptomatic or experience a self-limited illness, a severe form of COVID-19 develops in 3-21% of symptomatic patients depending on age, gender, race, and comorbidities (Wu and McGoogan, 2020). A fraction of severe COVID-19 patients (estimated at 17% to 35%) develops acute lung injury (ALI), acute respiratory distress syndrome (ARDS), and respiratory failure (World Health, 2020), associated with a 28-day all-cause mortality rate of 5-20% in face of standard of care (Beigel et al., 2020a; Horby et al., 2020). Survivors of severe COVID-19 are at risk of developing chronic complications including pulmonary fibrosis (Spagnolo et al., 2020).

The development of countermeasures that reduce COVID-19 morbidity and mortality has been an area of much global research. Since the development and approval of new drugs takes 8 to 12 years (DiMasi et al., 2016), off-label use of previously approved or investigational drugs has been the primary intervention modality. Unbiased high-throughput screens of compound libraries have recently discovered promising repurposing drug candidates that inhibit the replication of SARS-CoV-2 or the enzymatic activity of its proteins (Jin et al., 2020; Riva et al., 2020). Virtual (Choudhary et al., 2020; Richardson et al., 2020), interactomic (Gordon et al., 2020), and phosphoproteomic screens (Bouhaddou et al., 2020) have also facilitated the discovery of repurposing candidates.

The current standard of care for hospitalized patients requiring oxygen is corticosteroids, which mildly reduce mortality in these patients (Horby et al., 2020). IL-6 receptor antagonists provide additional mild benefit, particularly in early rapidly progressive disease (Gordon et al., 2021; Horby et al., 2021). Remdesivir, the only antiviral drug currently approved for hospitalized COVID-19 patients, does not appear to reduce mortality (Beigel et al., 2020b; Pan et al., 2020; Wang et al., 2020b). While trials assessing other countermeasures are ongoing, to date the reported clinical benefit has been overall limited (Saul and Einav, 2020). Moreover, no single agent capable of suppressing viral infection, inflammation and tissue injury has been identified. There is thus an urgent need for more effective approaches to prevent the acute and long-term complications associated with COVID-19 and ideally also provide readiness for future outbreaks of coronaviruses and unrelated emerging viruses.

To address these gaps, we conducted a stringent high-throughput screen of existing compounds for agents that rescue mammalian cells from SARS-CoV-2-induced lethality. Among the promising hits were inhibitors of members of the ErbB family of receptor tyrosine kinases (Finigan et al., 2012), including lapatinib, an approved anticancer drug. We provide support for the therapeutic potential of lapatinib and other pan-ErbB inhibitors as a broad-spectrum antiviral strategy and elucidate the molecular basis of its inhibition. Our findings provide evidence for regulation of SARS-CoV-2 infection and pathogenesis by ErbBs, validate ErbBs as druggable targets for antiviral and tissue protective approaches for COVID-19 and beyond, and propose

already approved (lapatinib and ibrutinib) and investigational (sapitinib) drugs with anti-pan-ErbB activity as an attractive class of repurposing candidates.

Results

High-throughput screening (HTS) for compounds that counteract SARS-CoV-2-induced lethality

We assembled a collection of 4,413 bioactive investigational compounds and FDA approved drugs largely derived from four commercially available libraries and a self-assembled set of 13 kinase inhibitors (**Figures 1A and S1A**). 3,550 of the compounds were unique, of which 749 were approved in humans and 18 in animals. This collection was screened at a final concentration of 10 µM in two independent experiments for inhibition of SARS-CoV-2 (Belgium-GHB-03021)-induced lethality in Vero E6 cells constitutively expressing an enhanced green fluorescent protein (eGFP) via a high-throughput assay, previously developed to identify anti-SARS-CoV inhibitors (Ivens et al., 2005b) (**Figure 1B**). The average percent area for control wells included in each plate were 102.9±5% for uninfected cells (cell control), 0.1±0.2% for infected untreated cells (virus control), and 0.0±0.164% for infected cells treated with DMSO (**Figure 1C**). The Z' and RZ' values of each of the 29 screen plates, calculated based on the virus control and cell control wells, were greater than 0.78 (**Figure S1B**). The signal-to-background (S/B) value, representing the ratio of the median value of the raw data between the virus control and the cell control, was greater than 120 (**Figure S1B**). The two replicate screens demonstrated good correlation (r= 0.76) (**Figure S1C**). Remdesivir and its major metabolite, GS-441524, used as positive controls, demonstrated dose-dependent anti-SARS-CoV-2 activity in this assay with EC_{50} (half-maximal effective concentration) values of 1.8-2.8 and 1.1-1.5 µM, respectively, and CC_{50} (half-maximal cellular cytotoxicity) greater than 50 µM (**Figure S1D)**. Overall, these data indicate that this antiviral assay is robust for HTS and is specific.

We set a percent area of greater than 15 in at least one of the two screens as the cutoff for positive hits (**Figures 1C and S1E**). 40 compounds from the commercial libraries and two from the self-assembled kinase inhibitor set met this criteria. Nelfinavir and salinomycin, but not ivermectin, previously demonstrating anti-SARS-CoV-2 activity (Ianevski et al., 2020; Saul and Einav, 2020), emerged by our more stringent assay. Eighteen of the 40 hits were prioritized based on PubChem data documenting lower promiscuity and toxicity or activity against other viruses (**Figure 1A**).

Dose-dependent effect of hits in an orthogonal antiviral assay

The 18 prioritized compounds were then studied for their dose-dependent effect on SARS-CoV-2 infection and cellular viability in Vero cells infected with a distinct viral isolate (2019-nCoV/USA-WA1/2020) via plaque and alamarBlue assays, respectively. 24 hour treatment with Ac-Leu-Leu-Nle-CHO, aurothioglucose, lapatinib, lycorine, calcimycin, tyrphostin AG 879, and azaserine showed potent dose-response antiviral activity with EC_{50}<0.7 µM, CC_{50}>20 µM, and selectivity indices (SI, CC_{50} to EC_{50} ratio) >29 (**Figures 1D, 1E and S1F**). Monesin, gedunin,

tetrandine, josamycin, sunitinib, and spiperone showed moderate antiviral activity beyond toxicity with EC_{50} values of 1.2-4.3 µM, CC_{50}>20 µM, and SI>5.1 (**Figures 1D and S1F**). Fluspirilene, loperamide, tyrphostin A9, and penitrem effectively suppressed SARS-CoV-2 infection without apparent toxicity at the tested concentrations, albeit with higher EC_{50} values of 15-18 µM (**Figures 1D and S1F**). Salbutamol showed no anti-SARS-CoV-2 activity (**Figures 1D and S1F**).

In total, 17 hits demonstrated antiviral effect beyond toxicity, and 12 of these were effective at sub to low micromolar concentrations. These compounds target diverse cellular factors and functions (**Figure 1F**). Two of the hits are known to target ErbBs: lapatinib (approved anticancer) (Chen et al., 2016) and tyrphostin AG 879 (experimental) (Levitzki and Gazit, 1995). Inhibitors of NUMB-associated kinases (NAK), heat shock protein 90 (HSP90) and ion transport across cell membranes were also among the hits. Five of the compounds have been approved either in the United States (lapatinib, sunitinib, aurothioglucose) or other countries (spiperone, josamycin), and seven are natural products (**Figure 1F**).

Broad-spectrum antiviral activity of hits

Next, we studied the broad-spectrum potential of the 18 emerging hits. The effect of these compounds on replication of two unrelated RNA viruses, TC-83, the vaccine strain of the alphavirus VEEV, and the flavivirus, dengue (DENV2) was measured in human astrocytes (U-87 MG) and human hepatoma (Huh7) cells, respectively, both via luciferase assays. Lycorine, calcimycin, monensin, azaserine, gedunin, and the kinase inhibitors lapatinib and AG 879 dose-dependently inhibited replication of TC-83 and DENV2 in addition to SARS-CoV-2 (**Figure S2**). Several compounds, such as tyrphostin A9, an investigational inhibitor of PDGFR (platelet-derived growth factor receptor), and fluspirilene, a neuroleptic agent, demonstrated more potent anti-TC-83 and DENV2 activity than anti-SARS-CoV-2 activity, and others showed variable activity against one or two of these viruses. Salbutamol demonstrated minimal to no activity against all three viruses (**Figure S2**).

Lapatinib has a broad-spectrum antiviral activity and a high genetic barrier to resistance

We focused on defining the therapeutic potential of lapatinib, an already approved pan-ErbB inhibitor that emerged in the screen (**Figure 2A**). Lapatinib dose-dependently inhibited replication of SARS-CoV-2 (USA-WA1/2020 strain) in both Vero and Calu-3 (human lung epithelial) cells at 24 hours post-infection with EC_{50} values of 0.5 µM and 0.7 µM, respectively, and CC_{50} >20 µM (**Figures 1E and 2B)**. Moreover, lapatinib demonstrated a dose-dependent rescue of Vero-eGFP cells from SARS-CoV-2-induced lethality at 96 hours post-infection (Belgium-GHB-03021 strain) (**Figures 2C and 2D**).

Next, we probed the effect of lapatinib on the replication of members of unrelated viral families: alphaviruses, flaviviruses and filoviruses. Beyond its observed anti-VEEV (TC-83) and anti-DENV2 effect via luciferase assays (**Figure S2**), lapatinib dose-dependently inhibited infections of both vaccine (TC-83) and wild type (WT) (Trinidad donkey, TrD) VEEV by plaque assays in

U-87 MG cells with EC_{50} values of 0.8 µM and CC_{50} >20 µM (**Figures 2E and 2F**). Similarly, lapatinib dose-dependently inhibited the replication of DENV2 (EC_{50}=1.8 µM) via plaque assays, and the filoviruses Ebola (EBOV) (EC_{50}=2.5 µM) and Marburg viruses (MARV) (EC_{50}=1.9 µM) via microneutralization assays in Huh7 cells, albeit lower CC_{50} values were measured in infected Huh7 cells (10.2-10.5 µM) relative to the other cell lines (**Figures 2G-2I**).

To determine whether viruses can escape treatment with lapatinib, we focused on VEEV (TC-83) since it replicates robustly in cultured cells, has a relatively short life cycle, and its handling does not require BSL3 containment. VEEV was passaged in U-87 MG cells in the presence of lapatinib or the VEEV nonstructural protein 2 (nsP2) inhibitor ML336 (Chung et al., 2010) at increasing concentrations corresponding to values between the EC_{50} and EC_{90}. Infectious virus production was measured in culture supernatants over several passages by plaque assays. By passage 3, VEEV overcame inhibition by ML336. In contrast, VEEV remained suppressed for 10 passages under the lapatinib treatment without phenotypic resistance (**Figure 2J**). Moreover, virus obtained from culture supernatants at passage 10 under lapatinib or DMSO treatment remained susceptible to lapatinib (**Figure 2K**). Conversely, virus obtained at passage 10 under ML336 treatment lost its susceptibility to ML336, with the emergence of a previously characterized resistance mutation in nsP2 (Y102C in VEEV TC-83), whereas virus obtained at the same passage under DMSO treatment remained susceptible to ML336 (**Figure 2L**).

These results point to lapatinib as a potential broad-spectrum antiviral agent with a higher relative barrier to resistance than a direct-acting antiviral, and support that lapatinib suppresses viral infection by targeting a cellular function.

Lapatinib inhibits SARS-CoV-2 entry

To understand lapatinib's target(s) and mechanism of antiviral action, we first tested the hypothesis that by targeting receptor tyrosine kinases, it inhibits the entry of vesicular stomatitis virus encapsidated RNA pseudotyped with the SARS-CoV-2 spike glycoprotein (rVSV-SARS-CoV-2-S). Treatment of Calu-3 and Vero cells with lapatinib dose-dependently suppressed rVSV-SARS-CoV-2-S infection measured by luciferase assays 24 hours post-infection without impacting cell viability (EC_{50}=2.6-3.2 µM, CC_{50} >20 µM) (**Figures 3A-3C**). Moreover, lapatinib suppressed the level of intracellular viral RNA at 3 hours post-infection of Vero cells with a high rVSV-SARS-CoV-2-S inoculum measured via RT-qPCR (**Figures 3A and 3D**). These results highlight a defect in the entry step, yet, it is possible that lapatinib inhibits additional, temporally distinct stages of the SARS-CoV-2 life cycle.

ErbB4, but not other lapatinib's targets, is essential for SARS-CoV-2 entry and VEEV (TC-83) infection

The ErbB family is composed of four members (ErbB1-4), of which three are catalytically active: ErbB1, 2 , and 4 (Finigan et al., 2012). Lapatinib's cancer targets are ErbB1 (EGFR) (IC_{50}=5.3 nM) and ErbB2 (HER2) (IC_{50}=35 nM) (Chen et al., 2016). Yet, its publicly available kinome (ID:20107) reveals potent binding to 5 additional kinases (ErbB4, RAF1, RIPK2, STK10, and

MAP2K5) at 0-30% of control, with an overall excellent selectivity. To define which of these 7 molecular targets mediate(s) the observed antiviral effect of lapatinib, we studied the effects of siRNA-mediated depletion of these kinases on rVSV-SARS-CoV-2-S and VEEV (TC-83) infections. Depletion of ErbBs by siRNA pools was confirmed (**Figure S3A and S3B**). ErbB4 depletion suppressed rVSV-SARS-CoV-2-S infection in Vero cells by 73% (**Figures 3E and 3F**) and VEEV (TC-83) infection in U-87 MG cells by 76% relative to non-targeting (NT) controls (**Figures 3G and 3H)**. RIPK2 depletion mildly reduced VEEV infection, but not rVSV-SARS-CoV-2-S infection (**Figures 3F and 3H**). Depletion of the remaining 5 targets, including ErbB1 and ErbB2, had no effect on infection of both viruses (**Figures 3F and 3H**). None of these siRNA pools impacted cellular viability (**Figures 3F and 3H**).

To further probe the functional relevance of ErbB4, we silenced ErbB4 expression in Vero and U-87 MG cells by two siRNAs targeting distinct regions in the ErbB4 transcript. Confirmed by RTqPCR, ErbB4 depletion by these siRNAs suppressed rVSV-SARS-CoV-2-S infection by 80-85% and VEEV (T-83) infection by 60-95% via luciferase assays relative to siNT (**Figures 3I-3L**). Moreover, these siErbB4s suppressed both virulent SARS-CoV-2 infection as measured via plaque assays by 78-97% and SARS-CoV-2 entry measured via quantification of intracellular viral RNA at 3 hours following high-inoculum infection by 50-80% relative to siNT (**Figures 3I, and 3M-3O)**. ErbB4 depletion did not impact cell viability (**Figures 3J, 3L and 3N**) and largely correlated with the observed phenotype. These findings confirm a role for ErbB4 in viral entry; a step of the viral life cycle, which is also inhibited by lapatinib.

Lapatinib was shown to bind the ATP binding site of ErbB4 in a comparable manner to ErbB1 and ErbB2 binding (Qiu et al., 2008). While an IC_{50} of 430 nM on ErbB4 was previously reported in a cell-free assay (Rusnak et al., 2001), we measured an IC_{50} of 28 nM with a different peptide substrate, and confirmed anti-ErbB2 activity (**Figures S3C)**.

To further probe the requirement for ErbBs in SARS-CoV-2 infection, we evaluated the antiviral effect of three other compounds with anti-ErbB activity. Tyrphostin AG 879, an experimental compound that emerged in the HTS (Levitzki and Gazit, 1995), dose-dependently inhibited SARS-CoV-2 and rVSV-SARS-CoV-2-S infections in Calu-3 cells, with EC_{50} of 0.5-1.1 µM and CC_{50}>20 µM (**Figures 3P and S3D**). Yet, its activity on ErbB2 and 4 could not be confirmed via the *in vitro* kinase assay (**Figures 3Q and S3C**), suggesting that another target may be mediating its antiviral activity. While not included in the original screen, ibrutinib, an approved anticancer Bruton's tyrosine kinase (BTK) inhibitor with potent, irreversible pan-ErbB activity (IC_{50}s: ErbB1=1.81 nM, ErbB2=12.1 nM, and ErbB4=1 nM) (Chen et al., 2016), suppressed both SARS-CoV-2 and rVSV-SARS-CoV-2-S infections, with EC_{50} of 1.3 µM and 1 µM and CC_{50}>20 µM (**Figures 3P, 3Q and S3E**). Similarly, Sapitinib, an investigational potent pan-ErbB inhibitor (IC_{50}s: ErbB1=12 nM, ErbB2=14 nM, and ErbB4=1.4 nM) demonstrated a dose-response effect on SARS-CoV-2 infection with an EC_{50} of 0.7 µM and CC_{50}>20 µM in Calu-3 cells and EC_{50} of 2.8 µM in Vero cells (**Figures 3P, 3Q and S3F**).

Collectively, these results provide evidence that ErbB4, but not ErbB1 or 2, is required for SARS-CoV-2 entry and VEEV (TC-83) infection, thereby validating it as a druggable antiviral

target. Its role as an entry co-factor, a step of the life cycle that is inhibited by lapatinib, supports a hypothesis that inhibition of ErbB4 mediates the antiviral effect of lapatinib.

ErbB4 is a molecular target mediating the antiviral effect of lapatinib

To determine whether lapatinib exerts its antiviral effect by inhibiting phosphorylation of the catalytically active ErbBs, lysates derived from SARS-CoV-2-infected Calu-3 cells treated with lapatinib or DMSO were subject to Western blot analysis. Lapatinib treatment dose-dependently suppressed the ratio of phosphorylated to total ErbB1, 2, and 4 levels at 24 hours post-infection with EC_{50} values lower than 0.1 μM that correlated with reduced expression of the SARS-CoV-2 nucleocapsid protein (**Figures 4A and 4B)**. Similar findings were observed at 1.5 hour post-infection (**Figures S4A and S4B**). These results provide evidence that drug exposure and the antiviral effect of lapatinib in these cells are correlated with functional inhibition of ErbBs' activity.

To confirm that inhibition of ErbB4 is a mechanism underlying the antiviral effect of lapatinib, we conducted gain-of-function assays. Ectopic expression of WT ErbB4, but not catalytically inactive ErbB4 mutant harboring a lysine to arginine substitution in position 751 (K751R) or control plasmid, either completely or partially reversed the antiviral effect of lapatinib on rVSV-SARS-CoV-2-S infection (**Figures 4C-4E and S4C**). Similarly, WT, but not the ErbB4 mutant, reversed the effect of lapatinib on VEEV (TC-83) infection (**Figures 4F-4H and S4D).** These results validate ErbB4 as a key mediator of the antiviral effect of lapatinib and indicate that its enzymatic activity is required for viral infection.

Taken together, these results indicate that ErbB4 is an antiviral target and a molecular target mediating the antiviral effect of lapatinib.

Lapatinib inhibits SARS-CoV-2-induced activation of ErbB-regulated inflammatory and tissue injury signals

Published animal and human data indicate that ErbB1 and 2 are key regulators of inflammation and tissue injury in both the acute and fibrotic phases of non-infectious ALI and ARDS (Faress et al., 2007; Finigan et al., 2012; Finigan et al., 2011; Finigan et al., 2015; Gasse et al., 2007; Hardie et al., 1996; Ma et al., 2020b; Madtes et al., 1999; Mitchell et al., 2011; Zhou et al., 2012) via activation of the p38 MAPK, AKT/mTOR and Ras/RAF/MEK/ERK pathways (Finigan et al., 2012; Finigan et al., 2011; Li et al., 2020a; Zarubin and Han, 2005; Zhang et al., 2016). In cultured cells, these ErbB-regulated pathways have been shown to be among the most strongly upregulated in SARS-CoV (Kopecky-Bromberg et al., 2006; Mizutani et al., 2004), MERS (Kindrachuk et al., 2015), and SARS-CoV-2 (Appelberg et al., 2020; Bouhaddou et al., 2020) infections. We therefore tested the hypothesis that lapatinib suppresses signaling in these downstream pathways via pan-ErbB inhibition. The phosphorylation level of AKT, p38 MAPK, and ERK was quantified by Western blot analysis in Calu-3 cell lysates harvested post-infection with SARS-CoV-2 and treatment with lapatinib. At 1.5 and 24 hours post-infection, SARS-CoV-2 increased the ratio of phosphorylated to total protein level of AKT, ERK, and/or p38 MAPK by

>1.5-2.5 fold (**Figure 5**), in agreement with prior reports in other cell lines (Appelberg et al., 2020; Bouhaddou et al., 2020; Mizutani et al., 2004). Notably, lapatinib treatment dramatically inhibited SARS-CoV-2-induced activation of AKT and ERK both at 1.5 and 24 hours post-infection and of p38 MAPK at 24 hours post-infection (**Figure 5**).

These results provide evidence that lapatinib inhibits activation of signaling pathways downstream of ErbBs, which are implicated in ALI and upregulated in pandemic coronaviral infections.

Lapatinib inhibits SARS-CoV-2 infection, inflammation, and tissue injury *ex vivo* in human lung organoids

To study the effect of lapatinib treatment on SARS-CoV-2 infection in a biologically relevant system, we used a human adult lung organoid (ALO) monolayer model that was recently validated. Generated from adult stem cells isolated from lung tissue, these organoids contain both proximal airway cells, critical for sustained viral infection, and distal alveolar cells (AT2→AT1), required for mounting the overzealous host immune response in fatal COVID-19 (Tindle et al., 2020) (**Figure 6A**). Viral replication measured by plaque assays in culture supernatant and nucleocapsid transcript expression measured by RT-qPCR in ALO monolayer lysates both peaked at 48 hours following SARS-CoV-2 infection (MOI=1) (**Figures S5A and S5B**), and were effectively suppressed by lapatinib, with EC_{50} values of 0.4 µM and <0.2 µM, respectively, and CC_{50} > 20 µM (**Figures 6A-6C**). Confocal immunofluorescence (IF) analysis at 24 hours post-infection revealed a near-complete disappearance of SARS-CoV-2 nucleocapsid staining in epithelial cell clusters forming alveolar-like structures and resembling AT2 cells in ALOs treated with 10 µM of lapatinib relative to DMSO controls (**Figures 6D and S5C**).

As in Calu-3 cells, lapatinib treatment dose-dependently inhibited phosphorylation of ErbB1, 2 and 4, indicating an association between its antiviral effect and ErbB modulation in these ALOs (**Figure 6E**). Moreover, lapatinib treatment inhibited SARS-CoV-2-induced phosphorylation of the downstream factors AKT and ERK, albeit not p38 MAPK, in this more complex tissue model at 48 hours post-infection (**Figure 6F**).

Next, we tested the hypothesis that by inhibiting this ErbB-regulated signaling in pathways implicated in inflammation, lapatinib suppresses the inflammatory response to SARS-CoV-2 infection. To do so, we studied the effect of lapatinib treatment on the level of cytokines in the ALO culture supernatants at 48 hours post-infection with SARS-CoV-2 using the LEGENDplex (Biolegend) flow cytometry-based cytokine beads array. SARS-CoV-2 infection increased the production of TNF-α, IL-1β and IL-6, in agreement with former reports (Del Valle et al., 2020). Lapatinib treatment dramatically dose-dependently reduced the expression level of these pro-inflammatory cytokines, with levels at or lower than those measured in uninfected organoids achieved at drug concentration of 0.5 µM (**Figure 6G**). Moreover, lapatinib treatment increased the expression level of MCP-1 (**Figure 6G**), suggesting that it may augment innate immune responses (Sokol and Luster, 2015).

Lastly, to define the effect of lapatinib on SARS-CoV-2-induced lung injury, we analyzed its effect on the integrity of tight junction formation in ALOs via confocal IF analysis. To minimize its direct antiviral effect, lapatinib was added to ALO monolayers 4 hours post-infection, i.e. at a post-entry stage. Claudin 7 staining of uninfected ALOs revealed a continuous membranous pattern with increased intensity on the basolateral membrane of cells surrounding the lumen of the alveolar-like structures (**Figures 6H, 6I, and S5D**). In contrast, 36 hours following SARS-CoV-2 infection and DMSO treatment, claudin 7 stained as speckles or short segments that often appeared in the cytoplasmic region rather than on the membrane. This finding was accompanied by cell separation and destruction of the alveolar-like architecture. ALOs treated with 10 µM of lapatinib exhibited an intact pattern of claudin 7 morphology and subcellular distribution and overall preserved architecture of the alveolar-like structure, comparable to the uninfected control samples (**Figures 6H, 6I and S5D).**

Together, these findings provide a proof of concept for the utility of pan-ErbB inhibitors in suppressing SARS-CoV-2 infection, inflammation and loss of epithelial barrier integrity in a model that recapitulates COVID-19 pathology.

Proposed model for the roles of ErbBs in the regulation of SARS-CoV-2 infection and pathogenesis and the mechanism of action of pan-ErbB inhibitors

Based on our and the cumulative published data (see Discussion), we propose a model wherein ErbB4 is required for SARS-CoV-2 entry, while pan-ErbB activation regulates signaling in downstream pathways that are upregulated in SARS-CoV-2 infection and implicated in ALI/ARDS and lung fibrosis. By suppressing both processes, pan-ErbB inhibitors, not only inhibit viral infection, but independently also reduce inflammation and tissue injury (**Figure 7**). Indeed, lapatinib was recently shown to maintain lung epithelium integrity in a non-infectious injury model induced by IL-1β, which activates the ErbB4 ligand NRG-1 via regulation of tight junction molecules (Ma et al., 2020b). Moreover, other ErbB1 and 2 inhibitors were shown to prevent or diminish lung alveolar permeability, vascular leak, lung remodeling, fibrosis, and mortality in various non-infectious animal models of lung injury (Bierman et al., 2008; Faress et al., 2007; Hardie et al., 2008b; Ishii et al., 2006). While it remains to be experimentally proven, since ErbB1 has been shown to be required for SARS-CoV infection (Freeman et al., 2014), and the pathways downstream of ErbBs are similarly upregulated in SARS-CoV and MERS, we predict that this model applies to other pandemic coronaviral infections.

Discussion

To address the unmet need for more effective antivirals, we conducted a stringent HTS of 4,413 existing compounds for agents that protect mammalian cells from SARS-CoV-2-induced lethality. Seventeen of the 18 emerging hits targeting a diverse repertoire of functions also showed anti-SARS-CoV-2 activity via plaque assays, and a subset of hits demonstrated a broad-spectrum antiviral potential. We integrated state of the art molecular virology, biochemistry, genetic, immunological, and pharmacological approaches with a unique human lung organoid model to define the therapeutic potential of lapatinib, an approved pan-ErbB

inhibitor, as an antiviral agent and characterize its mechanism of action. Our data support that lapatinib not only suppresses SARS-CoV-2 entry and VEEV infections via ErbB4 inhibition, but also inhibits pan-ErbB-mediated signaling in pathways implicated in inflammation and acute and chronic tissue injury. Lastly, we provide evidence that lapatinib reduces both inflammation and epithelial lung injury in human lung organoids and predict, based on published data, that inhibition of ErbB1 and 2 by lapatinib should also reduce lung fibrosis. Together, our data provide insights into the virus-host determinants that regulate SARS-CoV-2 infection and pathogenesis and illustrate the utility of a class of pan-ErbB inhibitors and unrelated compounds both as tools to identify antiviral drug targets and as candidate therapies against pandemic corona and other emerging viral infections.

Most antiviral strategies target viral enzymes, thereby typically providing a “one drug, one bug” approach that is prone to the emergence of viral resistance and is not easily scalable to meet the large unmet need (Bekerman and Einav, 2015; Saul and Einav, 2020). While drugs that target the viral polymerase, such as remdesivir and favipiravir, can suppress replication of unrelated viruses, the reported clinical benefit to date has been mild to moderate (Beigel et al., 2020b; Pan et al., 2020; Saul and Einav, 2020; Spinner et al., 2020; Wang et al., 2020b). Our data point to pan-ErbB inhibitors as broad-spectrum antiviral agents. Lapatinib has recently emerged in an independent screen for anti-SARS-CoV-2 compounds in human lung fibroblasts (Raymonda et al., 2020) and in an *in silico* screen (O’Donovan et al., 2021), but otherwise has not been studied for its antiviral activity or mechanism of antiviral action. Using orthogonal assays with two distinct SARS-CoV-2 isolates, we showed a potent effect of lapatinib in suppressing SARS-CoV-2 infection and rescuing cells from SARS-CoV-2-induced lethality. Lapatinib similarly suppressed replication of flaviviruses, alphaviruses and filoviruses, indicating its broad-spectrum potential and exhibited a higher relative barrier to resistance than a classical direct-acting antiviral.

Using lapatinib as a pharmacological tool, we discovered ErbB4, the least studied ErbB, as a candidate antiviral target. We then showed that ErbB4 is a co-factor of SARS-CoV-2 entry that is also required for VEEV (TC-83) infection, and that its kinase function is required for both infections. Unlike other ErbBs, to the best of our knowledge, ErbB4 has not been previously implicated in the life cycle of a virus. The precise role of ErbB4 in viral entry, either via fusion at the plasma membrane and/or endocytosis, remains to be elucidated. While writing this manuscript, ErbB4 was identified as a candidate interactor of the SARS-CoV-2 3C-like protease via an *in silico* approach (Selvaraj et al., 2021), suggesting that ErbBs may mediate later stages in the SARS-CoV-2 life cycle, as previously shown with ErbB1 in SARS-CoV infection (Freeman et al., 2014). Differential hijacking of ErbBs by distinct coronaviruses is also possible, however, by targeting all three catalytically active ErbBs, we predict that lapatinib will achieve pan-coronavirus coverage.

We provide multiple lines of evidence to support modulation of ErbB4 activity as an important mechanism of antiviral action of lapatinib in SARS-CoV-2 infection. We demonstrate that lapatinib inhibits viral entry, analogous to the phenotype seen with RNAi-mediated suppression of ErbB4. We establish that lapatinib’s antiviral activity correlates with reduced phospho-ErbB4

levels *in vitro*. In accordance with this finding, we show that WT but not a kinase dead ErbB4 mutant can rescue the antiviral effect of lapatinib against both SARS-CoV-2 entry and VEEV (TC-83) infection. This mechanism also plays a role *ex vivo* as evidenced by the correlation of antiviral activity with reduced ErbB4 phosphorylation in human lung organoids upon drug treatment. A block in ErbB4 phosphorylation thus mechanistically explains, at least in part, the antiviral effect of lapatinib and represents a useful pharmacodynamic biomarker to link between drug regimen, target effect, and antiviral response in future clinical studies.

Independent of the role we identified for ErbB4 in viral entry, we and others provide evidence that ErbBs are mediators of inflammation and lung injury. Human and animal data in multiple non-infectious models indicate that ErbBs are key regulators of ALI and the resulting fibrosis (Faress et al., 2007; Finigan et al., 2012; Finigan et al., 2011; Finigan et al., 2015; Gasse et al., 2007; Hardie et al., 1996; Ma et al., 2020b; Madtes et al., 1999; Mitchell et al., 2011; Zhou et al., 2012). In these models, ErbBs activate the p38 MAPK, AKT/mTOR and Ras/RAF/MEK/ERK pathways that play critical roles in ALI, ARDS and lung fibrosis (Bouhaddou et al., 2020; Saul and Einav, 2020). Similarly, transcriptomic and/or phosphoproteomic studies revealed that activation of ErbBs and/or these downstream pathways are among the strongest detected upon infection of human cells with SARS-CoV (Kopecky-Bromberg et al., 2006; Mizutani et al., 2004), SARS-CoV-2 (Appelberg et al., 2020; Bouhaddou et al., 2020) and MERS (Kindrachuk et al., 2015), and in mice infected with SARS-CoV (Venkataraman et al., 2017), supporting the roles of these pathways in pan-coronaviral infections and/or pathogenesis. In human lung epithelium and organoids, we demonstrate SARS-CoV-2-induced phosphorylation of p38 MAPK, AKT, and ERK and lapatinib-mediated inhibition of both ErbB phosphorylation and activation of these deleterious signaling pathways downstream of ErbBs.

ErbB-mediated activation of the p38 MAPK, AKT/mTOR and Ras/RAF/MEK/ERK pathways causes secretion of pro-inflammatory cytokines, loss of epithelial barrier function, thrombosis, and vasoconstriction (Finigan et al., 2012; Finigan et al., 2011; Li et al., 2020a; Zarubin and Han, 2005; Zhang et al., 2016)—processes also involved in severe COVID-19 pathogenesis (Lee and Choi, 2021; Saul and Einav, 2020). In various animal models of ALI/ARDS, ErbB2 activation disrupts epithelial barrier function (Finigan et al., 2012; Finigan et al., 2011) by controlling cell-cell adhesion (Finigan et al., 2015) and tight junctions (Ma et al., 2020b; Mitchell et al., 2011). In humans with ALI, the level of the ErbB4 ligand, NRG-1 is elevated in bronchoalveolar lavage fluid and plasma and correlates with disease severity (Finigan et al., 2011). Beyond NRG-1, which is regulated in part by IL-1β, ErbBs mediate the deleterious effects of at least three additional ligands implicated in ALI and lung fibrosis, some of which have been shown to be relevant in coronaviral infections: transforming growth factor alpha (TGF-α), heparin-binding EGF-like growth factor (HB-EGF), and amphiregulin (AREG) (Finigan et al., 2011; Gasse et al., 2007; Hardie et al., 1996; Li et al., 2016; Madtes et al., 1999; Zhou et al., 2012). It is also intriguing to speculate that the imbalance in the renin angiotensin system (RAS), thought to play a major role in the pathogenesis of severe coronaviral infections (Kassiri et al., 2009; Kuba et al., 2005; Lee and Choi, 2021; Oudit et al., 2009; Saul and Einav, 2020), contributes to the observed activation of ErbB pathways. Indeed, unopposed Angiotensin (Ang) II effect was shown to activate ErbBs and their downstream pathways (Forrester et al., 2016;

Gschwind et al., 2001; Koka et al., 2008; Mugabe et al., 2010; Ohtsu et al., 2006; Tang et al., 2000), and was linked to increased pulmonary vascular permeability in animal models of non-viral lung injury (Kassiri et al., 2009; Simões e Silva et al., 2013). In contrast, Ang (1–7) was shown to exert its protective effects via the Mas receptor by acting as a pan-ErbB inhibitor (Akhtar et al., 2015; Akhtar et al., 2012). Moreover, blocking the RAS pathway was shown to reverse ALI in mice injected with the spike Fc-protein of SARS-CoV (Kuba et al., 2005) and reduce inflammation in other disease models (Liu et al., 2014). Other approaches that target individual components of these pathways are being studied currently for COVID-19 treatment including Ang (1-7) peptides, antibodies targeting IL-1β, TGF-β and IL-6, and p38 MAPK inhibitors. By inhibiting the activation of ErbBs by multiple ligands and Ang II, lapatinib should, at least in theory, achieve a greater anti-inflammatory and tissue protective effect. Lastly, its ErbB4-mediated antiviral effect is unique (**Figure 7**).

In agreement with studies in COVID-19 patients (Del Valle et al., 2020), we provide evidence that SARS-CoV-2 infection increases production of the pro-inflammatory cytokines IL-1β, TNF-α and IL-6 in human lung organoids. Importantly, lapatinib treatment dose-dependently inhibited the production of these cytokines and concurrently increased the level of MCP-1, suggesting that it may also augment innate immune responses (Sokol and Luster, 2015). Our IF data provides evidence for the potential utility of laptinib in maintaining lung epithelial barrier integrity. We predict that the anti-inflammatory and tissue protective effects of lapatinib are beyond its ErbB4-mediated antiviral effect. First, these effects correlate with suppression of relevant signaling pathways. Second, the tissue protective effect was observed when the drug was added 4 hours post-infection, i.e. following the first round of viral entry. Third, lapatinib was shown to reverse increased lung epithelium permeability in a non-infectious model (Ma et al., 2020b). Fourth, while lapatinib has not been previously studied in mouse models of ALI, AG1478, an investigational ErbB1 inhibitor diminished lung alveolar permeability, vascular leak, and neutrophil accumulation in the BAL in a mouse model of mechanical ventilation-induced ALI (Bierman et al., 2008).

Beyond ALI, ErbB1 and 2 are implicated in the chronic sequela of lung fibrosis (Finigan et al., 2015; Gasse et al., 2007; Hardie et al., 1996; Madtes et al., 1999; Zhou et al., 2012). Most relevant, ErbB1 was shown to mediate SARS-CoV-induced fibrosis independently of virus titers in a STAT1-/- mouse model (Venkataraman et al., 2017). Notably, various ErbB inhibitors, including a humanized monoclonal antibody targeting ErbB2 (2C4), and the ErbB1 inhibitors gefitinib, erlotinib and AG1478 reduced lung fibrosis, morbidity and/or mortality in bleomycin- and TGF-α induced lung fibrosis mouse models (Faress et al., 2007; Hardie et al., 2008a; Ishii et al., 2006). Based on these cumulative data, we predict that lapatinib may protect from these chronic complications of coronaviral infections.

Collectively, these findings provide insight into the mechanisms underlying the antiviral, anti-inflammatory, and tissue protective effects of lapatinib. The repurposed approaches being studied for COVID-19 to date typically target one of these processes, but not all three. Demonstrating potent antiviral, anti-inflammatory, and tissue protective effects in the biologically relevant human ALO model provides important insight into the translatability of this approach.

While lapatinib has not been studied for COVID-19 treatment to date, ibrutinib has recently shown protection from progression to severe COVID-19, albeit in a small number of patients (Treon et al., 2020). Yet, this effect was attributed solely to ibrutinib's anti-inflammatory effect via its cancer target, BTK. Nevertheless, beyond its anti-BTK activity, ibrutinib is a potent pan-ErbB inhibitor (Chen et al., 2016) (**Figure 3Q**). Indeed, we show that like lapatinib, ibrutinib inhibits SARS-CoV-2 infection and viral entry. While it is possible that BTK plays a role in SARS-CoV-2 infection and/or pathogenesis, our data provide evidence that the pan-ErbB inhibition by ibrutinib likely mediates, at least in part, the observed protective effect. Our findings thus provide insight into the mechanism of action of another repurposed candidate for COVID-19 and propose additional investigational pan-ErbB inhibitor candidates (e.g. sapitinib).

Repurposing existing drugs requires significantly less capital and time and diminishes the clinical risks, as such drugs have already been tested (toxicity, pharmacokinetics (PK), pharmacodynamics, dosing, etc.) for their primary indication (Saul and Einav, 2020). Lapatinib is a once-daily oral drug that is approved globally in combination drug treatments for metastatic, ErbB2-positive breast cancer. Based on the available PK data, the plasma level achieved with the approved anti-cancer dose of lapatinib (1500 mg once daily) is 8-10 fold higher than the EC_{50}s we measured for its anti-SARS-CoV-2 effect in mammalian cells and human lung organoids. Moreover, the lung to plasma area under the curve ratio of lapatinib in mice and humans is 10 and 8.2, respectively (Hudachek and Gustafson, 2013), indicating that it should sustain even higher levels in this most relevant tissue.

Although toxicity is a concern when targeting host functions, finding a safe therapeutic window may be feasible. Lapatinib has a favorable safety profile, particularly when used as a monotherapy and for short durations, as those required to treat acute infections. Notably, the largest safety database based on which the toxicity profile in lapatinib's package insert was determined is based on data from over 12,000 patients with advanced cancer who received lapatinib in combination with capecitabine or trastuzumab plus an aromatase inhibitor and for long durations (Novartis, 2018). In pivotal trials, the most commonly reported adverse events reported more frequently with combination therapy including lapatinib compared with capecitabine or trastuzumab monotherapy were diarrhea, palmar-plantar erythrodysesthesia, nausea, vomiting, stomatitis, and rash (Novartis, 2018; Pivot et al., 2015; Schwartzberg et al., 2010). Most of these adverse events were mild or moderate in intensity, with diarrhea being the most common adverse event resulting in drug discontinuation. The most common laboratory abnormalities with combination therapy were increased liver function tests with infrequent increases of grade 3 or higher severity (Novartis, 2018; Piccart-Gebhart et al., 2016; Pivot et al., 2015; Schwartzberg et al., 2010). As monotherapy, lapatinib was tested in several open-label studies at doses up to 1600 mg/day with a median duration of 7-28 weeks in patients with advanced cancer. These studies reported that the most common adverse events were rash, diarrhea, nausea, pruritus, fatigue, with no grade 4 adverse events (Blackwell et al., 2010; Blackwell et al., 2009; Burris et al., 2005; Burstein et al., 2008; Gomez et al., 2008; Hurvitz and Kakkar, 2012; Perez et al., 2008; Toi et al., 2009). Diarrhea was the most common grade 3 adverse event, occurring in 9% of patients in some studies (Blackwell et al., 2009). More severe

adverse events including transient and reversible decreases in left ventricular ejection fraction, prolongation of QT interval, and hepatotoxicity, were also documented, yet infrequently, and with the exception of cardiac toxicity, primarily in patients receiving lapatinib in combination treatment (Dogan et al., 2012; Kloth et al., 2015; Novartis, 2018; Perez et al., 2008).

Notably, unlike the other receptor tyrosine kinase inhibitors erlotinib and gefitinib, lapatinib monotherapy has not been associated with pneumonitis, interstitial lung disease or lung fibrosis (Blackwell et al., 2010; Blackwell et al., 2009; Burris et al., 2005; Burstein et al., 2008; Gomez et al., 2008; Hurvitz and Kakkar, 2012; Perez et al., 2008; Toi et al., 2009). The estimated incidence of 0.2% for these adverse effects is based on 8 cases reported in three phase 3 clinical trials and several additional case reports, all in patients receiving lapatinib in combination with other drugs (Bates et al., 2019a; Brenner et al., 2010; Capri et al., 2010; Hackshaw et al., 2020; Jagiello-Gruszfeld et al., 2010; Xu et al., 2011) known to cause pneumonitis and/or lung fibrosis (Bielopolski et al., 2017; Chan et al., 2011; Torrisi et al., 2011), and sometimes also with radiation, for a median duration of 24-45 weeks. We predict that the distinct off-target profile of lapatinib compared with erlotinib and gefitinib accounts for the difference in the occurrence of these adverse events. Indeed, cyclin G-associated kinase (GAK), an off-target of erlotinib (K_D=3.1 nM, IC_{50}=0.88 µM) and gefitinib (K_D=6.5 nM, IC_{50}=0.41 µM), but not of lapatinib (K_D=980 nM, IC_{50}>5 µM)(Asquith et al., 2020), has been implicated in pulmonary alveolar function and alveolar epithelial stem cell regeneration, and its inhibition is thought to be the mechanism underlying gefinitib- and erlotinib- induced lung toxicity (Bates et al., 2019b; Tabara et al., 2011). These findings, combined with the large body of published data in multiple animal models of ALI/ARDS and lung fibrosis showing a clear role for ErbB1 and 2 in disease pathogenesis and benefit for their pharmacological inhibition, support a lung protective effect for lapatinib.

An important consideration with lapatinib is, however, its potential for drug-drug interactions. Since metabolized by CYP3A4, concurrent use of suppressors of CYP3A4 should be avoided to reduce risk of QT prolongation. Concurrent treatment with strong inducers of CYP3A4 should also be avoided, as this can reduce lapatinib's levels to sub-therapeutic. Of particular relevance is dexamethasone, standard of care for moderate COVID-19 patients, which induces CYP3A4. Since other steroids do not induce CYP3A4, lapatinib could be studied in combination with hydrocortisone or prednisone, which have been shown to achieve a comparable protective effect in SARS-CoV-2 patients (Dequin et al., 2020; Group, 2020; Investigators, 2020).

Another kinase inhibitor that emerged in the HTS was sunitinib, an approved anticancer multi-kinase inhibitor that we have previously shown to protect mice from DENV and EBOV challenges when given in combination with erlotinib by inhibiting NAK-mediated intracellular viral trafficking (Bekerman et al., 2017; Neveu et al., 2012; Pu et al., 2020). Sunitinib was recently shown to suppress pan-corona pseudotyped viral infections (Wang et al., 2020a). Tyrphostin AG 879 demonstrated potent anti-SARS-CoV-2 activity and was previously shown to suppress replication of multiple viruses including a mouse hepatitis virus (Coronaviridae) in cultured cells and to protect mice from influenza A virus (IAV) challenge (Kumar et al., 2011a; Kumar et al.,

2011b; Zoeller and Geoghegan-Barek, 2019). Nevertheless, since we could not confirm its anti-ErbB activity, the precise target(s) mediating the antiviral effect remain to be elucidated.

Beyond kinases, diverse cellular functions emerged in our HTS as candidate targets for anti-SARS-CoV-2 approaches. One example is ion transport across cell membranes. Among the hits was tetrandine, a calcium channel blocker with anti-inflammatory and anti-fibrogenic properties used as a medicinal herb for the treatment of lung silicosis, liver cirrhosis, and rheumatoid arthritis (Kwan and Achike, 2002). Tetrandine was previously shown to inhibit entry of EBOV in cultured cells and protect EBOV-infected mice by inhibiting endosomal calcium channels (Sakurai et al., 2015). Monensin sodium, an antiprotozoal agent, and calcimycin, previously shown to inhibit VSV and IAV infections (Marois et al., 2014; Onishi et al., 1991), are both ionophores that facilitate the transport of sodium/potassium and calcium across the membrane, respectively. Spiperone hydrochloride, an activator of calcium-activated chloride channels licensed in Japan for the treatment of schizophrenia, was another hit.

The emergence of gedunin, a natural product that inhibits HSP90 and has anti-inflammatory properties, in the screen suggests a potential role for HSP90 in SARS-CoV-2 infection, similarly to other viral infections (Amraiz D, 2017; Geller et al., 2012). Lycorine was also previously shown to suppress replication of multiple viruses including SARS-CoV in cultured cells (Ieven et al., 1983; Li et al., 2005; Szlávik et al., 2004; Yang et al., 2019) and mortality of mice infected with human enterovirus 71 (Liu et al., 2011). The underlying mechanism of action in influenza was thought to be inhibition of export of viral ribonucleoprotein complexes from the nucleus (Yang et al., 2019), yet lycorine also exhibits anti-inflammatory effects (Li et al., 2020b). Azaserine is a natural serine derivative that irreversibly inhibits γ-glutamyltransferase in the metabolic hexosamine pathway. Independently of this target, it was shown to protect from endothelial cell inflammation and injury by reducing reactive oxygen species and downregulating VCAM-1 and ICAM-1 expression in response to TNF-α (Rajapakse et al., 2009). Aurothioglucose has been previously used for the treatment of rheumatoid arthritis and was thought to inhibit the activity of adenylyl cyclase in pro-inflammatory pathways (Botz et al., 2014). While it recently emerged as a potential inhibitor of the SARS-CoV-2 3C-like protease, since the IC_{50} was 13.32 μM, this is unlikely to be the mechanism of antiviral action (Baker et al., 2021). Ac-Leu-Leu-Nle-CHO is a competitive inhibitor of the neutral, calcium-dependent cysteine proteases calpain 1 and 2 (CAPN1 and 2) used as a research tool. Targeting various calpain proteases was shown to inhibit SARS-CoV-2 (Ma et al., 2020a), SARS-CoV (Barnard et al., 2004) and IAV replication (Blanc et al., 2016) as well as the activation of latent HIV infection (Teranishi et al., 2003). While inhibition of the viral protease (M^{pro}) could be one mechanism of action (Ma et al., 2020a), since CAPN1 and 2 were shown to be required for SARS-CoV infection (Schneider et al., 2012), echovirus 1 (Upla et al., 2008) and herpes simplex virus nuclear transport (Zheng et al., 2014), inhibition of these cellular targets may also play a role. Moreover, calpain inhibition was shown to exert anti-inflammatory and tissue protective effects (Li et al., 2009; Supinski and Callahan, 2010) including in a reovirus-induced myocarditis mouse model (DeBiasi et al., 2001), and thus may add another potential value. Lastly, josamycin is a natural macrolide antibiotic used in humans in Europe and Japan. Interestingly, other macrolide inhibitors have been shown to suppress IAV replication and reduce inflammation

(Sugamata et al., 2014). These findings reveal candidate targets for anti-SARS-CoV-2 approaches. Moreover, they underscore the potential utility of natural products as broad-spectrum antivirals, yet limited scalability typically challenges the use of these products.

In summary, our study reveals candidate broad-spectrum antiviral therapies that target a variety of cellular functions via repurposing. It illuminates regulation of coronaviral and alphaviral infections and disease pathogenesis by ErbBs and defines the therapeutic potential and mechanism of action of lapatinib, which not only suppresses viral replication, but also protects from inflammation and tissue injury. The safety and efficacy of pan-ErbB inhibition by lapatinib and/or other agents warrants clinical evaluation and may position us to combat COVID-19, newly emerging coronaviruses, and other emerging viruses, thereby providing readiness for future outbreaks. Lastly, we reveal the utility of a unique propagable, cost effective, and personalized, ALO model that may be effectively applied for "*ex vivo* clinical trials".

Acknowledgements

This work was supported by a gift from Frank Quattrone and Denise Foderaro (to SE), award number HDTRA11810039 from the Defense Threat Reduction Agency (DTRA)/Fundamental Research to Counter Weapons of Mass Destruction (to SE, SDJ and AN), award number W81XWH-16-1-0691 from the Department of Defense (DoD)/Congressionally Directed Medical Research Programs (CDMRP) (to SE and SDJ), and by the National Institutes for Health (NIH) grants 3R01DK107585-05S1 (to SD), UCOP-R00RG2642 (to SD and PG), and UCOP-R01RG3780 (to PG and DS). Flow cytometry analysis and IF confocal microscopy for this project were done on instruments in the Stanford Shared FACS Facility and Stanford Cell Science Imaging Facility (CSIF) respectively. We thank the Stanford SPARK program's advisors for critical advice and investigators who have provided plasmids (see Methods). We also thank the staff of Stanford Clinical Virology Laboratory for their help sequencing the SARS-CoV-2 USA-WA1/2020 isolate used in this work. Opinions, conclusions, interpretations, and recommendations are those of the authors and are not necessarily endorsed by the U.S. Army. The mention of trade names or commercial products does not constitute endorsement or recommendation for use by the Department of the Army or the Department of Defense.

Author Contributions

S.S., M.K, P.T.H, L.G., W.C., S.K, P.L., N.B, C.C., K.H, M.L., M.S. designed and performed the experiments and conducted data analysis. C.T., S.D., P.G., D.S.C, J.J., provided reagents and guidance. S.E., S.D.J., J.D., D.J., J.N, A.N, and B.A.P. provided scientific oversight and guidance. S.E, S.S., S.D.J, M.K. W.C, and D.J. wrote the first version of the manuscript. S.E., D.J., J.N., A.N., S.D.J. provided funding for the studies.

Declaration of interest

The authors declare no competing interests.

Methods:

Compound libraries and reagents. The 4 commercial libraries (Microsource Spectrum library of 2000 compounds, the two Biomol collections of 480 known diverse bioactive compounds with defined biological activity and 640 FDA-approved drugs, and the LOPAC collection of 1280 pharma-developed tools and approved drugs) were available at the Stanford High-Throughput Bioscience Center. Small molecule inhibitors were purchased from MedchemExpress or from Cayman Chemical except for Ac-Leu-Leu-Nle-CHO (BML-P120, Enzo Life Sciences), tesevatinib (A110575, Adooq Bioscience LLC), and erlotinib (E-4007, LC Laboratories). Dinaciclib and ribociclib were a gift from Dr. Mardo Koivomaegi (Stanford University).

High-throughput screening (HTS) of compound libraries. Compounds from the libraries listed above were plated in a total of 29 assay-ready 384-well plates (Greiner #7810192). Dispensing of 6 µl of the compound solutions was achieved using an automated Agilent Bravo pipetting system, allowing for a final test concentration of 10 µM (or 10-20 in the case of the self-assembled kinase inhibitor collection). The HTS was based on an assay previously developed to discover antiviral agents for SARS-CoV infection (Ivens et al., 2005a). Briefly, 30 µL Vero-E6-eGFP cells were added at 8000 cells/well to columns 1-24 24 hours before infection. 30 µL assay medium was added to columns 23 and 24, which were used as cell controls. Following a 20-hour incubation, cells in columns 1-22 were infected with 30 µL SARS-CoV-2 (Belgium-GHB-03021) at an MOI of 0.001, using an automated, no-contact liquid handler (EVO 100, Tecan) on the Caps-It robotics system. Plates were then incubated for 4 days and imaged via a high content imager (Arrayscan XTI, Thermofisher) using wide-field fluorescence microscopy. eGFP signal was used as a marker for survival from viral-induced lethality. The cells were excited at 485-20 nm and emission was captured via a CCD camera and a BGRFRN_BGRFRN dichroic mirror and filter set. A 5X objective was used so that 1 single image contains approximately 75% of a well surface. The exposure time was set at 0.023 seconds, as determined by the fluorescent intensity signal in the control wells. Imaging acquisition speed was optimized using a 2x2 binning on 1104x1104 pixel resolution and reducing the number of autofocus focal planes. The Cellomics (Thermofisher) software was used for image analysis. A custom-made image analysis protocol was created using the SpotDetector bioapplication. First, a background reduction was performed on the raw images to remove non-specific fluorescent signal. Second, a fixed fluorescent intensity threshold was determined to identify eGFP signal. Lastly, the total surface area occupied by eGFP signal was calculated from the processed images. The selected output feature was ‘SpotTotalAreaCh2’ and was used for further data analysis.

Hit selection. The entire compound collection was screened in two independent experiments. Data were normalized to the median of each plate. The *Z*-score was calculated on the basis of the log2(fold change) (log2FC) with the average and standard deviation of each plate. 40 compounds from the screen were selected according to the cutoff of fluorescence % area greater than 15 in at least one of the two screens, which is 15 times greater than the values obtained with untreated or DMSO treated cells.

Plasmids. Plasmids used in the production of SARS-CoV-2 pseudovirus were a gift from Jing Lin (Vitalant, San Francisco). Plasmid encoding VEEV TC-83 with a nanoluciferase reporter (VEEV TC-83-Cap-nLuc-Tav) was a gift from Dr. William B. Klimstra (Department of Immunology, University of Pittsburgh) (Sun et al., 2014). DENV2 (New Guinea C strain) TSV01 Renilla reporter plasmid (pACYC NGC FL) was a gift from Pei-Yong Shi (University of Texas Medical Branch, Galveston, Texas, USA) (Zou et al., 2011). pDONR223-ErbB4 was a gift from William Hahn & David Root (Addgene plasmid # 23875 ; http://n2t.net/addgene:23875 ; RRID:Addgene_23875) (Johannessen et al., 2010). The ORF was recombined into a gateway compatible pGluc destination vector using Gateway technology (Invitrogen) and the construct was verified using Sanger sequencing. Mutations were introduced by site-directed mutagenesis using the QuikChange Lightning Site-Directed Mutagenesis Kit (Agilent).

Viral stocks preparation and/or passaging. Belgium-GHB-03021 SARS-CoV-2 strain was recovered from a nasopharyngeal swab taken from an asymptomatic patient returning from Wuhan, China early February 2020 (Spiteri et al., 2020) and passaged 6 times on Huh7 and Vero E6 cells. Viral titer was quantified by means of endpoint titrations on confluent Vero E6 cell cultures, calculated using the Spearman-Kärber method, and expressed as 50% tissue culture infectious dose ($TCID_{50}$)/ml. All Belgium-GHB-03021 SARS-CoV-2-related work was conducted in the high-containment BSL3+ facilities of the KU Leuven Rega Institute (3CAPS) under licenses AMV 30112018 SBB 219 2018 0892 and AMV 23102017 SBB 219 2017 0589 according to institutional guidelines.

The USA-WA1/2020 SARS-CoV-2 strain was received from BEI Resources and passaged 3-6 times in Vero E6 cells in DMEM supplemented with 2% FBS. Viral stock titers were determined by standard plaque assay on Vero E6 cells, as described (Case et al., 2020).

VEEV-TC-83-nLuc RNA was transcribed *in vitro* from cDNA plasmid templates linearized with MluI via MEGAscript SP6 kit (Invitrogen #AM1330) and electroporated into BHK-21 cells. Similarly, DENV RNA was transcribed *in vitro* from pACYC-DENV2-NGC plasmid by mMessage/mMachine (Ambion) kits and electroporated into BHK-21 cells. For both viruses, the supernatants were harvested after 24 hours post electroporation, clarified and stored at -80 °C. WT Trinidad Donkey (TrD) VEEV strain, EBOV (Kikwit isolate) and MARV (Ci67 strain) were obtained from BEI Resources. EBOV and MARV were grown in Vero E6 cells. Viral stock titers were determined via standard plaque assays on BHK-21 for DENV and VEEV or on Vero E6 cells for EBOV and MARV.

USA-WA1/2020 SARS-CoV-2- and WT VEEV-related work was conducted in the high-containment BSL3 facilities of Stanford University and George Mason University according to CDC and institutional guidelines. EBOV and MARV work was conducted at the high-containment BSL4 facilities at the United States Army Medical Research Institute of Infectious Diseases.

Viral sequencing. All SARS-CoV-2 stocks were deep sequenced on a MiSeq platform (Illumina).

For the HTS of compound library, Belgium/GHB-03021/2020 SARS-CoV-2 from passage 6 (P6) was used. The viral stock was deep sequenced following an established metagenomics pipeline (Boudewijns et al., 2020). 100% of the viral reads of P6 GHB-03021/2020 SARS-CoV-2 harbored a deletion of the multi-basic cleavage (MBC) domain, as reported (Boudewijns et al., 2020).

The rest of the experiments were done using the USA-WA1/2020 strain. SARS-CoV-2 whole-genome amplicon-based sequencing was conducted by adapting an existing whole genome sequencing pipeline for poliovirus genotyping (Sahoo et al., 2017). Dose response curves with lapatinib in Vero and Calu-3 cells (**Figures 1E and 2B**, respectively) were performed with a P3 USA-WA1/2020 SARS-CoV-2 virus harboring no deletion or point mutations in the MBC domain. The remaining experiments were performed using a P6 USA-WA1/2020 SARS-CoV-2 containing mixed populations, of which the majority (>51%) had WT sequence with no MBC deletion.

Cells. The African green monkey kidney cell line (Vero E6) constitutively expressing the enhanced green fluorescent protein (eGFP) used for antiviral screening purposes was kindly provided by Dr. Marnix Van Loock (Janssen Pharmaceutica, Beerse, Belgium)(Ivens et al., 2005a). Cells were maintained in Dulbecco's modified Eagle's medium (DMEM; Gibco) supplemented with 10% v/v fetal calf serum (FCS; Biowest), 0.075% sodium bicarbonate (7.5% solution, Gibco) and 1x Pen-strep (Gibco). The assay medium was DMEM, supplemented with 2% FCS. Vero E6 (ATCC) were maintained in DMEM (10-013-CV, Corning) supplemented with 10% fetal bovine serum (FBS, Omega Scientific, Inc), 1% L-glutamine 200mM (Gibco), 1% penicillin-streptomycin (Gibco), 1% nonessential amino acids (Gibco), 1% HEPES (Gibco), 1% Sodium pyruvate (Thermofisher scientific). Vero (ATCC), HEK-293T (ATCC), U-87 MG (ATCC), and BHK-21 (ATCC) cells were grown in DMEM (10-013-CV, Corning) supplemented with 10% FBS (Omega Scinetific, Inc), and 1% penicillin-streptomycin. Huh7 cells (Apath LLC) and Calu-3 cells (ATCC) were grown in DMEM (10-013-CV, Corning) supplemented with 10% FBS (Omega Scinetific, Inc), 1% l-glutamine, 1% nonessential amino acids (Corning) and 1% penicillin-streptomycin (Gibco). All the cells were maintained in a humidified incubator with 5% CO_2 at 37°C. All cells were tested negative for mycoplasma by the MycoAlert mycoplasma detection kit (Lonza, Morristown, NJ).

Human adult lung organoids and organoid-derived monolayers for SARS-CoV-2 infection. The human adult lung organoid (ALO) model containing proximal and distal features of airway epithelia was generated from adult stem cells isolated from deep lung biopsy specimens (Tindle et al., 2020). The organoids from these lung tissues were isolated and propagated using an approved human research protocol (IRB# 190105: PI Ghosh and Das) that covers human subject research at the UC San Diego HUMANOID Center of Research Excellence (CoRE). The lung organoid model is complete with all 6 cell types of proximal and distal airways as validated previously (Tindle et al., 2020). Lung-organoid-derived single cells were prepared (Tindle et al., 2020) and plated in Pneumacult Ex-Plus Medium (StemCell, Canada). After 2 days, monolayers were infected with SARS-CoV-2 (USA-WA1/2020 strain) at an MOI of 1.

rVSV-SARS-CoV-2-S production. HEK-293T cells were transfected with 30 µg of Spike (S) expression plasmid. Twenty-four hours post-transfection, the medium was replaced and cells were treated with DMEM containing 3.75 mM valproic acid (VPA) for 4 hours. The medium was then removed, and cells were infected with VSV-G pseudotyped ΔG-luciferase VSV virus (MOI=3). Six hours post-infection, cells were washed with PBS and fresh medium containing anti-VSV-G hybridoma was added to neutralize the residual VSV-G pseudovirus. Culture supernatant was harvested after 24-hour incubation, clarified by centrifugation, filtered (0.22 µm) and stored at -80°C. The $TCID_{50}$ of rVSV-SARS-CoV-2-S pseudovirus was determined via luciferase assay 24 hours after infection of Vero cells. Positive wells were defined as having luminescence unit (RLU) values at least 10-fold higher than the cell background.

Western blotting and antibodies*.* Cells were lysed in M-Per protein extraction reagent (Thermo Fisher Scientific) or RIPA buffer containing 1% NP40 supplemented with Halt protease and phosphatase inhibitor cocktail (Thermo Fisher Scientific). Clarified lysates were run on 4%–12% Bis-Tris gels (Invitrogen), transferred onto PVDF membranes (Bio-Rad). Blots were blocked with 5% BSA/TBST and blotted with anti-ErbB4 (Santa Cruz), ErbB2 (Cell Signaling), ErbB1, AKT, ERK, p38 (Cell Signaling), P-ErbB4 (Tyr1284), P-ErbB2(Tyr1248), P-AKT(Ser473), P-ERK(Thr202/Tyr204), P-p38 (Thr180/Tyr182) (Cell Signaling), and β-actin (Sigma-Aldrich, catalog A3854) antibodies. Signal was detected with HRP-conjugated secondary antibodies. Band intensity was quantified with ImageJ software (NIH).

RNA interference. siRNAs (10 pmol/96-well) were transfected into cells using lipofectamine RNAiMAX transfection reagent (Invitrogen) 48 hours prior to infection with VEEV-TC-83-nLuc at MOI of 0.01, rVSV-SARS-CoV-2-S or SARS-CoV-2 (USA-WA1/2020). ON-TARGETPlus siRNA SMARTpools against 7 genes and non-targeting siRNA (siNT) were purchased from Dharmacon/Horizon Discovery with gene IDs as follows: EGFR (1956), ErbB2 (2064), ErbB4 (2066), RIPK2 (8767), RAF1 (5894), STK10 (6793), MAP2K5 (5607). Single ErbB4 siRNAs were ordered from Millipore Sigma (ErbB#1 GCAAGAAUUGACUCGAAU, ErbB#2 CCUCAAAGAUACCUAGUUA).

Infection assays. Calu-3 cells, Vero cells or ALOs were infected with SARS-CoV-2 in triplicates (MOI=0.05 or 1) in DMEM containing 2% FCS at 37°C under biosafety level 3 (BSL3) conditions. After 1 to 3-hour incubation, the inoculum was removed, cells were washed and supplemented with new medium. At various time points post-infection, culture supernatants were harvested for measurement of viral titer by standard plaque assays and cells were lysed in Trizol for RT-qPCR analysis. Huh7 cells were infected with DENV2 in replicates (n = 3-10) at an MOI of 0.05. Overall infection was measured at 48 hours using a *Renilla* luciferase substrate or a standard plaque assay. Huh7 cells were infected with EBOV (MOI=1) or MARV (MOI=2) under BSL4 conditions. 48 hours post-infection cells were formalin-fixed for 24 hours prior to removal from BSL4. Infected cells were detected using an EBOV or MARV glycoprotein-specific monoclonal antibody (KZ52 and 7E6, respectively) and quantitated by automated fluorescence microscopy using an Operetta High Content Imaging System and the Harmony software package (PerkinElmer). U-87 MG cells were infected with VEEV-TC-83-nLuc in 8 replicates at MOI of 0.01. Overall infection was measured at 24 hours post-infection via a nanoluciferase

assay using a luciferin solution obtained from the hydrolysis of its O-acetylated precursor, hikarazine-103 (prepared by Dr. Yves Janin, Institut Pasteur, France) as a substrate(Coutant et al., 2019) or standard plaque assay. U-87 MG cells were infected with WT VEEV TrD in triplicates and at 24 hours post-infection the viral titer was measured via standard plaque assays.

Pharmacological inhibition. Inhibitors or DMSO were added to the cells 1 hour prior to viral inoculation and were left for the duration of the experiment. Viral infection was measured via luciferase (DENV2, VEEV (TC-83)) or plaque (SARS-CoV-2, VEEV-TrD, VEEV (TC-83), DENV2) assays. Immunofluorescence assay with anti-GP probe was used for EBOV and MARV.

Entry assays. Vero cells were infected with virulent SARS-CoV-2 (MOI=1) or a high inoculum of rVSV-SARS-CoV-2-S. Following 1-hour incubation, the viral inoculum was removed, cells were washed three times with PBS and replaced with fresh medium. At 3 hours post-infection, cells were lysed in TRIzol (Invitrogen) or RLT lysis buffer (RNeasy Mini Kit, Qiagen) and viral RNA levels were measured by RT-qPCR.

RT-qPCR. RNA was extracted from cell lysates using Direct-zol RNA Miniprep Plus Kit (Zymo Research) or RNeasy Mini Kit (Qiagen) and reverse transcribed using High-Capacity cDNA RT kit (Applied Biosystems) according to the manufacturer's instructions. Primers and PowerUp SYBR Green Master Mix (Applied Biosystems) were added to the samples, and PCR reactions were performed with QuantStudio3 (Applied Biosystems). Samples were analyzed in triplicates and target genes were normalized to the housekeeping gene. The following primers were used: GAPDH (F-GGAGCGAGATCCCTCCAAAAT; R-GGCTGTTGTCATACTTCTCATGG), ErbB1 (F-ACCACCCTGGTCTGGAAGTACG; R-TCGTTGGACAGCCTTCAAGACC); ErbB2 (F-GGAAGTACACGATGCGGAGACT; R-ACCTTCCTCAGCTCCGTCTCTT); ErbB4 (F-GGAGTATGTCCACGAGCACAAG; R-CGAGTCGTCTTTCTTCCAGGTAC) N-SARS-CoV2 (F-TAATCAGACAAGGAACTGATTA, R-CGAAGGTGTGACTTCCATG).

Viability assays. Viability was assessed using alamarBlue reagent (Invitrogen) according to the manufacturer's protocol. Fluorescence was detected at 560 nm on an InfiniteM1000 plate reader (Tecan).

Gain-of-function assays. Plasmids encoding WT ErbB4, ErbB4 mutant (K751R) or empty control were transfected individually into Vero or U-87 MG cells using Lipofectamine 3000 reagent (Invitrogen) 24 hours prior to drug treatment and infection with rVSV-SARS-CoV-2-S or VEEV-TC-83-nLuc, respectively. Viral infection and cell viability were measured 24 hours later via luciferase and alamarBlue assays, respectively.

Resistance studies. VEEV (TC-83) was used to inoculate U-87 MG cells at MOI of 0.1 and passaged every 24 hours by transferring an equal volume of viral supernatant to naive cells under increasing drug selection (2.5-5 μM, passages 1–3; 5-10 μM, passages 4-7; 10-15 μM, passages 8-10). Upon completion of 10 passages, viral titers were measured in culture

supernatants by plaque assays. ML336 resistant mutation emerging in nsP2 at passage 10 was confirmed by purification and reverse transcription of viral RNA from cell supernatants using RNeasy Mini Kit (Qiagen) and SuperScript IV First-Strand Synthesis kit (Invitrogen) respectively. The nsP2 region was amplified with Platinum Green Hot Start PCR Master Mix (2x) (Invitrogen) using the following primers: (forward: AGGAAAATGTTAGAGGAGCACAAG reverse: GTCAATATACAGGGTCTCTACGGGGTGT (and sequenced (Sequetech Corp.).

In vitro kinase assays. ErbB2 and ErbB4 *in vitro* kinase assays were performed on the LabChip platform (Nanosyn) or radiometric HotSpot^{TM} kinase assay platform (Reaction Biology).

Signaling pathway analysis. Following a 2-hour starvation under serum-low or -free conditions(Sutton et al., 2013), Calu-3 cells or ALOs were treated with lapatinib or DMSO and within an hour infected with SARS-CoV-2 (MOI=1). Cell lysates were obtained at 1.5 and/or 24 hours post-infection followed by Western blot analysis with antibodies targeting the phosphorylated and total forms of ErbB1, 2 and 4, p38/MAPK, ERK, and AKT, as described(Zona et al., 2013). Phosphorylated to total protein ratios were quantified with ImageJ software (NIH).

Cytokine measurements in culture supernatants. A LEGENDplex Human Inflammation Panel 1 (Biolegend) kit was used following the manufacturer's instructions to measure the concentration of cytokines in culture supernatants derived from ALOs. Cytokine concentrations were measured via Quanteon (Agilent) and data analyzed using LEGENDplex V8.0 software.

Immunofluorescence and confocal microscopy. ALO cells were plated at a concentration of 2.5×10^6 cell/well in a μ-Slide 8 well (ibidi) system. Lapatinib or DMSO were administered either an hour pre-infection or 4 hours post-infection with SARS-CoV-2 (MOI=1). At 24-, 36- and 48-hours post-infection, cells were washed with PBS and fixed with 4% PFA for 30 minutes at RT. Cells were blocked for 1h at RT with 3% BSA and 0.1 % Triton X in PBS. Cells were incubated with mouse mAb SARS-CoV-2 nucleocapsid antibody (SinoBiological, 1:100) and rabbit Claudin 7 polyclonal antibody (ThermoFisher, 1:200) overnight at 4°C, followed by 1 hour incubation at room temperature with goat anti-mouse AF488 (ThermoFisher, 1:400), goat anti-rabbit AF647 (ThermoFisher, 1:400), and counterstaining with DAPI (4', 6-diamidino-2-phenylindole, ThermoFisher, 1:10000) and phalloidin (ThermoFisher, 1:400). Images were taken on an SP8 microscope (Leica). Adjustment for brightness, contrast and color balance were done using Fiji software.

Quantification and Statistical Analysis. All data were analyzed with GraphPad Prism software. Fifty percent effective concentrations (EC_{50}) and 50% cytotoxic concentration (CC_{50}) were measured by fitting of data to a 3-parameter logistic curve. *P* values were calculated by one-way ANOVA with either Dunnett's or Tukey's multiple comparisons tests as specified in each figure legend.

References:

Akhtar, S., Chandrasekhar, B., Attur, S., Dhaunsi, G.S., Yousif, M.H.M., and Benter, I.F. (2015). Transactivation of ErbB Family of Receptor Tyrosine Kinases Is Inhibited by Angiotensin-(1-7) via Its Mas Receptor. PloS one *10*, e0141657-e0141657.

Akhtar, S., Yousif, M.H.M., Dhaunsi, G.S., Chandrasekhar, B., Al-Farsi, O., and Benter, I.F. (2012). Angiotensin-(1-7) inhibits epidermal growth factor receptor transactivation via a Mas receptor-dependent pathway. Br J Pharmacol *165*, 1390-1400.

Amraiz D, Z.N., Fatima M (2017). Antiviral evaluation of an Hsp90 inhibitor, gedunin, against dengue virus. . Trop J Pharm Res *16*, 997-1004.

Appelberg, S., Gupta, S., Svensson Akusjärvi, S., Ambikan, A.T., Mikaeloff, F., Saccon, E., Végvári, Á., Benfeitas, R., Sperk, M., Ståhlberg, M.*, et al.* (2020). Dysregulation in Akt/mTOR/HIF-1 signaling identified by proteo-transcriptomics of SARS-CoV-2 infected cells. Emerging Microbes & Infections *9*, 1748-1760.

Asquith, C.R.M., Laitinen, T., Bennett, J.M., Wells, C.I., Elkins, J.M., Zuercher, W.J., Tizzard, G.J., and Poso, A. (2020). Design and Analysis of the 4-Anilinoquin(az)oline Kinase Inhibition Profiles of GAK/SLK/STK10 Using Quantitative Structure-Activity Relationships. ChemMedChem *15*, 26-49.

Baker, J.D., Uhrich, R.L., Kraemer, G.C., Love, J.E., and Kraemer, B.C. (2021). A drug repurposing screen identifies hepatitis C antivirals as inhibitors of the SARS-CoV2 main protease. PLOS ONE *16*, e0245962.

Barnard, D.L., Hubbard, V.D., Burton, J., Smee, D.F., Morrey, J.D., Otto, M.J., and Sidwell, R.W. (2004). Inhibition of severe acute respiratory syndrome-associated coronavirus (SARSCoV) by calpain inhibitors and beta-D-N4-hydroxycytidine. Antiviral chemistry & chemotherapy *15*, 15-22.

Bates, C.A., Zhao, B., Schlobohm, A., Asquith, C., Zuercher, W., and Barkauskas, C. (2019a). Inhibition of Cyclin G-Associated Kinase (GAK) Impairs Growth of Alveolar Type 2 Cells in a 3-Dimensional Culture System.

Bates, C.A., Zhao, B., Schlobohm, A., Asquith, C., Zuercher, W., and Barkauskas, C.E. (2019b). Inhibition of Cyclin G-Associated Kinase (GAK) Impairs Growth of Alveolar Type 2 Cells in a 3-Dimensional Culture System. In A61 EPITHELIAL BIOLOGY (American Thoracic Society), pp. A2125-A2125.

Beigel, J.H., Tomashek, K.M., Dodd, L.E., Mehta, A.K., Zingman, B.S., Kalil, A.C., Hohmann, E., Chu, H.Y., Luetkemeyer, A., Kline, S.*, et al.* (2020a). Remdesivir for the Treatment of Covid-19 - Final Report. The New England journal of medicine, NEJMoa2007764.

Beigel, J.H., Tomashek, K.M., Dodd, L.E., Mehta, A.K., Zingman, B.S., Kalil, A.C., Hohmann, E., Chu, H.Y., Luetkemeyer, A., Kline, S.*, et al.* (2020b). Remdesivir for the Treatment of Covid-19 - Final Report. The New England journal of medicine *383*, 1813-1826.

Bekerman, E., and Einav, S. (2015). Combating emerging viral threats. Science *348*, 282-283.

Bekerman, E., Neveu, G., Shulla, A., Brannan, J., Pu, S.-Y., Wang, S., Xiao, F., Barouch-Bentov, R., Bakken, R.R., Mateo, R.*, et al.* (2017). Anticancer kinase inhibitors impair intracellular viral trafficking and exert broad-spectrum antiviral effects. The Journal of clinical investigation *127*.

Bielopolski, D., Evron, E., Moreh-Rahav, O., Landes, M., Stemmer, S.M., and Salamon, F. (2017). Paclitaxel-induced pneumonitis in patients with breast cancer: case series and review of the literature. Journal of chemotherapy (Florence, Italy) *29*, 113-117.

Bierman, A., Yerrapureddy, A., Reddy, N.M., Hassoun, P.M., and Reddy, S.P. (2008). Epidermal growth factor receptor (EGFR) regulates mechanical ventilation-induced lung injury in mice. Transl Res *152*, 265-272.

Blackwell, K.L., Burstein, H.J., Storniolo, A.M., Rugo, H., Sledge, G., Koehler, M., Ellis, C., Casey, M., Vukelja, S., Bischoff, J.*, et al.* (2010). Randomized study of Lapatinib alone or in combination with trastuzumab in women with ErbB2-positive, trastuzumab-refractory metastatic breast cancer. J Clin Oncol *28*, 1124-1130.

Blackwell, K.L., Pegram, M.D., Tan-Chiu, E., Schwartzberg, L.S., Arbushites, M.C., Maltzman, J.D., Forster, J.K., Rubin, S.D., Stein, S.H., and Burstein, H.J. (2009). Single-agent lapatinib for HER2-overexpressing advanced or metastatic breast cancer that progressed on first- or second-line trastuzumab-containing regimens. Ann Oncol *20*, 1026-1031.

Blanc, F., Furio, L., Moisy, D., Yen, H.L., Chignard, M., Letavernier, E., Naffakh, N., Mok, C.K., and Si-Tahar, M. (2016). Targeting host calpain proteases decreases influenza A virus infection. American journal of physiology Lung cellular and molecular physiology *310*, L689-699.

Botz, B., Bölcskei, K., Kereskai, L., Kovács, M., Németh, T., Szigeti, K., Horváth, I., Máthé, D., Kovács, N., Hashimoto, H.*, et al.* (2014). Differential regulatory role of pituitary adenylate cyclase-activating polypeptide in the serum-transfer arthritis model. Arthritis & rheumatology (Hoboken, NJ) *66*, 2739-2750.

Boudewijns, R., Thibaut, H.J., Kaptein, S.J.F., Li, R., Vergote, V., Seldeslachts, L., De Keyzer, C., Sharma, S., Jansen, S., Weyenbergh, J.V.*, et al.* (2020). STAT2 signaling as double-edged sword restricting viral dissemination but driving severe pneumonia in SARS-CoV-2 infected hamsters. bioRxiv, 2020.2004.2023.056838.

Bouhaddou, M., Memon, D., Meyer, B., White, K.M., Rezelj, V.V., Correa Marrero, M., Polacco, B.J., Melnyk, J.E., Ulferts, S., Kaake, R.M.*, et al.* (2020). The Global Phosphorylation Landscape of SARS-CoV-2 Infection. Cell *182*, 685-712.e619.

Brenner, T., Motsch, J., Werner, J., Grenacher, L., Martin, E., and Hofer, S. (2010). Rapid-Onset Acute Respiratory Distress Syndrome (ARDS) in a Patient Undergoing Metastatic Liver Resection: A Case Report and Review of the Literature. Anesthesiol Res Pract *2010*, 586425.

Burris, H.A., 3rd, Hurwitz, H.I., Dees, E.C., Dowlati, A., Blackwell, K.L., O'Neil, B., Marcom, P.K., Ellis, M.J., Overmoyer, B., Jones, S.F.*, et al.* (2005). Phase I safety, pharmacokinetics, and clinical activity study of lapatinib (GW572016), a reversible dual inhibitor of epidermal growth factor receptor tyrosine kinases, in heavily pretreated patients with metastatic carcinomas. J Clin Oncol *23*, 5305-5313.

Burstein, H.J., Storniolo, A.M., Franco, S., Forster, J., Stein, S., Rubin, S., Salazar, V.M., and Blackwell, K.L. (2008). A phase II study of lapatinib monotherapy in chemotherapy-refractory HER2-positive and HER2-negative advanced or metastatic breast cancer. Ann Oncol *19*, 1068-1074.

Capri, G., Chang, J., Chen, S.C., Conte, P., Cwiertka, K., Jerusalem, G., Jiang, Z., Johnston, S., Kaufman, B., Link, J.*, et al.* (2010). An open-label expanded access study of lapatinib and capecitabine in patients with HER2-overexpressing locally advanced or metastatic breast cancer. Ann Oncol *21*, 474-480.

Case, J.B., Bailey, A.L., Kim, A.S., Chen, R.E., and Diamond, M.S. (2020). Growth, detection, quantification, and inactivation of SARS-CoV-2. Virology *548*, 39-48.

Chan, A.K., Choo, B.A., and Glaholm, J. (2011). Pulmonary toxicity with oxaliplatin and capecitabine/5-Fluorouracil chemotherapy: a case report and review of the literature. Onkologie *34*, 443-446.

Chen, J., Kinoshita, T., Sukbuntherng, J., Chang, B.Y., and Elias, L. (2016). Ibrutinib Inhibits ERBB Receptor Tyrosine Kinases and HER2-Amplified Breast Cancer Cell Growth. Mol Cancer Ther *15*, 2835-2844.

Choudhary, S., Malik, Y.S., and Tomar, S. (2020). Identification of SARS-CoV-2 Cell Entry Inhibitors by Drug Repurposing Using in silico Structure-Based Virtual Screening Approach. Frontiers in Immunology *11*.

Chung, D., Schroeder, C.E., Sotsky, J., Yao, T., Roy, S., Smith, R.A., Tower, N.A., Noah, J.W., McKellip, S., Sosa, M.*, et al.* (2010). ML336: Development of Quinazolinone-Based Inhibitors Against Venezuelan Equine Encephalitis Virus (VEEV). In Probe Reports from the NIH Molecular Libraries Program (Bethesda (MD): National Center for Biotechnology Information (US)).

Coutant, E.P., Goyard, S., Hervin, V., Gagnot, G., Baatallah, R., Jacob, Y., Rose, T., and Janin, Y.L. (2019). Gram-scale synthesis of luciferins derived from coelenterazine and original insights into their bioluminescence properties. Organic & biomolecular chemistry *17*, 3709-3713.

DeBiasi, R.L., Edelstein, C.L., Sherry, B., and Tyler, K.L. (2001). Calpain inhibition protects against virus-induced apoptotic myocardial injury. J Virol *75*, 351-361.

Del Valle, D.M., Kim-Schulze, S., Huang, H.-H., Beckmann, N.D., Nirenberg, S., Wang, B., Lavin, Y., Swartz, T.H., Madduri, D., Stock, A.*, et al.* (2020). An inflammatory cytokine signature predicts COVID-19 severity and survival. Nature medicine *26*, 1636-1643.

Dequin, P.-F., Heming, N., Meziani, F., Plantefève, G., Voiriot, G., Badié, J., François, B., Aubron, C., Ricard, J.-D., Ehrmann, S.*, et al.* (2020). Effect of Hydrocortisone on 21-Day Mortality or Respiratory Support Among Critically Ill Patients With COVID-19: A Randomized Clinical Trial. JAMA *324*, 1298-1306.

DiMasi, J.A., Grabowski, H.G., and Hansen, R.W. (2016). Innovation in the pharmaceutical industry: New estimates of R&D costs. Journal of health economics *47*, 20-33.

Dogan, E., Yorgun, H., Petekkaya, I., Ozer, N., Altundag, K., and Ozisik, Y. (2012). Evaluation of cardiac safety of lapatinib therapy for ErbB2-positive metastatic breast cancer: a single center experience. Medical oncology (Northwood, London, England) *29*, 3232-3239.

Faress, J.A., Nethery, D.E., Kern, E.F., Eisenberg, R., Jacono, F.J., Allen, C.L., and Kern, J.A. (2007). Bleomycin-induced pulmonary fibrosis is attenuated by a monoclonal antibody targeting HER2. Journal of applied physiology (Bethesda, Md : 1985) *103*, 2077-2083.

Finigan, J.H., Downey, G.P., and Kern, J.A. (2012). Human epidermal growth factor receptor signaling in acute lung injury. American journal of respiratory cell and molecular biology *47*, 395-404.

Finigan, J.H., Faress, J.A., Wilkinson, E., Mishra, R.S., Nethery, D.E., Wyler, D., Shatat, M., Ware, L.B., Matthay, M.A., Mason, R.*, et al.* (2011). Neuregulin-1-human epidermal receptor-2 signaling is a central regulator of pulmonary epithelial permeability and acute lung injury. The Journal of biological chemistry *286*, 10660-10670.

Finigan, J.H., Vasu, V.T., Thaikoottathil, J.V., Mishra, R., Shatat, M.A., Mason, R.J., and Kern, J.A. (2015). HER2 activation results in β-catenin-dependent changes in pulmonary epithelial permeability. American journal of physiology Lung cellular and molecular physiology *308*, L199-207.

Forrester, S.J., Kawai, T., O'Brien, S., Thomas, W., Harris, R.C., and Eguchi, S. (2016). Epidermal Growth Factor Receptor Transactivation: Mechanisms, Pathophysiology, and Potential Therapies in the Cardiovascular System. Annual Review of Pharmacology and Toxicology *56*, 627-653.

Freeman, M.C., Peek, C.T., Becker, M.M., Smith, E.C., and Denison, M.R. (2014). Coronaviruses Induce Entry-Independent, Continuous Macropinocytosis. mBio *5*, e01340-01314.

Gasse, P., Mary, C., Guenon, I., Noulin, N., Charron, S., Schnyder-Candrian, S., Schnyder, B., Akira, S., Quesniaux, V.F.J., Lagente, V.*, et al.* (2007). IL-1R1/MyD88 signaling and the inflammasome are essential in pulmonary inflammation and fibrosis in mice. The Journal of clinical investigation *117*, 3786-3799.

Geller, R., Taguwa, S., and Frydman, J. (2012). Broad action of Hsp90 as a host chaperone required for viral replication. Biochimica et biophysica acta *1823*, 698-706.

Gomez, H.L., Doval, D.C., Chavez, M.A., Ang, P.C.-S., Aziz, Z., Nag, S., Ng, C., Franco, S.X., Chow, L.W.C., Arbushites, M.C.*, et al.* (2008). Efficacy and Safety of Lapatinib As First-Line Therapy for ErbB2-Amplified Locally Advanced or Metastatic Breast Cancer. Journal of Clinical Oncology *26*, 2999-3005.

Gordon, A.C., Mouncey, P.R., Al-Beidh, F., Rowan, K.M., Nichol, A.D., Arabi, Y.M., Annane, D., Beane, A., van Bentum-Puijk, W., Berry, L.R.*, et al.* (2021). Interleukin-6 Receptor Antagonists in Critically Ill Patients with Covid-19 – Preliminary report. medRxiv, 2021.2001.2007.21249390.

Gordon, D.E., Jang, G.M., Bouhaddou, M., Xu, J., Obernier, K., White, K.M., O'Meara, M.J., Rezelj, V.V., Guo, J.Z., Swaney, D.L.*, et al.* (2020). A SARS-CoV-2 protein interaction map reveals targets for drug repurposing. Nature *583*, 459-468.

Group, T.W.R.E.A.f.C.-T.W. (2020). Association Between Administration of Systemic Corticosteroids and Mortality Among Critically Ill Patients With COVID-19: A Meta-analysis. JAMA *324*, 1330-1341.

Gschwind, A., Zwick, E., Prenzel, N., Leserer, M., and Ullrich, A. (2001). Cell communication networks: epidermal growth factor receptor transactivation as the paradigm for interreceptor signal transmission. Oncogene *20*, 1594-1600.

Hackshaw, M.D., Danysh, H.E., Singh, J., Ritchey, M.E., Ladner, A., Taitt, C., Camidge, D.R., Iwata, H., and Powell, C.A. (2020). Incidence of pneumonitis/interstitial lung disease induced by HER2-targeting therapy for HER2-positive metastatic breast cancer. Breast cancer research and treatment *183*, 23-39.

Hardie, W.D., Davidson, C., Ikegami, M., Leikauf, G.D., Cras, T.D.L., Prestridge, A., Whitsett, J.A., and Korfhagen, T.R. (2008a). EGF receptor tyrosine kinase inhibitors diminish transforming growth factor-α-induced pulmonary fibrosis. American Journal of Physiology-Lung Cellular and Molecular Physiology *294*, L1217-L1225.

Hardie, W.D., Davidson, C., Ikegami, M., Leikauf, G.D., Le Cras, T.D., Prestridge, A., Whitsett, J.A., and Korfhagen, T.R. (2008b). EGF receptor tyrosine kinase inhibitors diminish transforming growth factor-alpha-induced pulmonary fibrosis. American journal of physiology Lung cellular and molecular physiology *294*, L1217-1225.

Hardie, W.D., Kerlakian, C.B., Bruno, M.D., Huelsman, K.M., Wert, S.E., Glasser, S.W., Whitsett, J.A., and Korfhagen, T.R. (1996). Reversal of lung lesions in transgenic transforming growth factor alpha mice by expression of mutant epidermal growth factor receptor. American journal of respiratory cell and molecular biology *15*, 499-508.

Horby, P., Lim, W.S., Emberson, J.R., Mafham, M., Bell, J.L., Linsell, L., Staplin, N., Brightling, C., Ustianowski, A., Elmahi, E.*, et al.* (2020). Dexamethasone in Hospitalized Patients with Covid-19 - Preliminary Report. The New England journal of medicine.

Horby, P.W., Pessoa-Amorim, G., Peto, L., Brightling, C.E., Sarkar, R., Thomas, K., Jeebun, V., Ashish, A., Tully, R., Chadwick, D.*, et al.* (2021). Tocilizumab in patients admitted to hospital with COVID-19 (RECOVERY): preliminary results of a randomised, controlled, open-label, platform trial. medRxiv, 2021.2002.2011.21249258.

Hudachek, S.F., and Gustafson, D.L. (2013). Physiologically based pharmacokinetic model of lapatinib developed in mice and scaled to humans. Journal of pharmacokinetics and pharmacodynamics *40*, 157-176.

Hurvitz, S.A., and Kakkar, R. (2012). Role of lapatinib alone or in combination in the treatment of HER2-positive breast cancer. Breast Cancer (Dove Med Press) *4*, 35-51.

Ianevski, A., Yao, R., Fenstad, M.H., Biza, S., Zusinaite, E., Reisberg, T., Lysvand, H., Løseth, K., Landsem, V.M., Malmring, J.F.*, et al.* (2020). Potential Antiviral Options against SARS-CoV-2 Infection. Viruses *12*.

Ieven, M., van den Berghe, D.A., and Vlietinck, A.J. (1983). Plant antiviral agents. IV. Influence of lycorine on growth pattern of three animal viruses. Planta medica *49*, 109-114.

Investigators, T.W.C.f.t.R.-C. (2020). Effect of Hydrocortisone on Mortality and Organ Support in Patients With Severe COVID-19: The REMAP-CAP COVID-19 Corticosteroid Domain Randomized Clinical Trial. JAMA *324*, 1317-1329.

Ishii, Y., Fujimoto, S., and Fukuda, T. (2006). Gefitinib prevents bleomycin-induced lung fibrosis in mice. American journal of respiratory and critical care medicine *174*, 550-556.

Ivens, T., Eynde, C.V.d., Acker, K.V., Nijs, E., Dams, G., Bettens, E., Ohagen, A., Pauwels, R., and Hertogs, K. (2005a). Development of a homogeneous screening assay for automated detection of antiviral agents active against severe acute respiratory syndrome-associated coronavirus. Journal of virological methods *129*, 56-63.

Ivens, T., Van den Eynde, C., Van Acker, K., Nijs, E., Dams, G., Bettens, E., Ohagen, A., Pauwels, R., and Hertogs, K. (2005b). Development of a homogeneous screening assay for automated detection of antiviral agents active against severe acute respiratory syndrome-associated coronavirus. J Virol Methods *129*, 56-63.

Jagiello-Gruszfeld, A., Tjulandin, S., Dobrovolskaya, N., Manikhas, A., Pienkowski, T., DeSilvio, M., Ridderheim, M., and Abbey, R. (2010). A single-arm phase II trial of first-line paclitaxel in combination with lapatinib in HER2-overexpressing metastatic breast cancer. Oncology *79*, 129-135.

Jin, Z., Du, X., Xu, Y., Deng, Y., Liu, M., Zhao, Y., Zhang, B., Li, X., Zhang, L., Peng, C.*, et al.* (2020). Structure of Mpro from COVID-19 virus and discovery of its inhibitors. Nature.

Johannessen, C.M., Boehm, J.S., Kim, S.Y., Thomas, S.R., Wardwell, L., Johnson, L.A., Emery, C.M., Stransky, N., Cogdill, A.P., Barretina, J.*, et al.* (2010). COT drives resistance to RAF inhibition through MAP kinase pathway reactivation. Nature *468*, 968-972.

Kassiri, Z., Zhong, J., Guo, D., Basu, R., Wang, X., Liu, P.P., Scholey, J.W., Penninger, J.M., and Oudit, G.Y. (2009). Loss of angiotensin-converting enzyme 2 accelerates maladaptive left ventricular remodeling in response to myocardial infarction. Circulation Heart failure *2*, 446-455.

Kindrachuk, J., Ork, B., Hart, B.J., Mazur, S., Holbrook, M.R., Frieman, M.B., Traynor, D., Johnson, R.F., Dyall, J., Kuhn, J.H.*, et al.* (2015). Antiviral Potential of ERK/MAPK and PI3K/AKT/mTOR Signaling Modulation for Middle East Respiratory Syndrome Coronavirus Infection as Identified by Temporal Kinome Analysis. Antimicrobial agents and chemotherapy *59*, 1088-1099.

Kloth, J.S.L., Pagani, A., Verboom, M.C., Malovini, A., Napolitano, C., Kruit, W.H.J., Sleijfer, S., Steeghs, N., Zambelli, A., and Mathijssen, R.H.J. (2015). Incidence and relevance of QTc-interval prolongation caused by tyrosine kinase inhibitors. British journal of cancer *112*, 1011-1016.

Koka, V., Huang, X.R., Chung, A.C., Wang, W., Truong, L.D., and Lan, H.Y. (2008). Angiotensin II up-regulates angiotensin I-converting enzyme (ACE), but down-regulates ACE2 via the AT1-ERK/p38 MAP kinase pathway. The American journal of pathology *172*, 1174-1183.

Kopecky-Bromberg, S.A., Martinez-Sobrido, L., and Palese, P. (2006). 7a protein of severe acute respiratory syndrome coronavirus inhibits cellular protein synthesis and activates p38 mitogen-activated protein kinase. Journal of virology *80*, 785-793.

Kuba, K., Imai, Y., Rao, S., Gao, H., Guo, F., Guan, B., Huan, Y., Yang, P., Zhang, Y., Deng, W.*, et al.* (2005). A crucial role of angiotensin converting enzyme 2 (ACE2) in SARS coronavirus–induced lung injury. Nature medicine *11*, 875-879.

Kumar, N., Liang, Y., Parslow, T.G., and Liang, Y. (2011a). Receptor Tyrosine Kinase Inhibitors Block Multiple Steps of Influenza A Virus Replication. Journal of virology *85*, 2818-2827.

Kumar, N., Sharma, N.R., Ly, H., Parslow, T.G., and Liang, Y. (2011b). Receptor tyrosine kinase inhibitors that block replication of influenza a and other viruses. Antimicrobial agents and chemotherapy *55*, 5553-5559.

Kwan, C.Y., and Achike, F.I. (2002). Tetrandrine and related bis-benzylisoquinoline alkaloids from medicinal herbs: cardiovascular effects and mechanisms of action. Acta pharmacologica Sinica *23*, 1057-1068.

Lee, C., and Choi, W.J. (2021). Overview of COVID-19 inflammatory pathogenesis from the therapeutic perspective. Archives of pharmacal research *44*, 99-116.

Levitzki, A., and Gazit, A. (1995). Tyrosine kinase inhibition: an approach to drug development. Science *267*, 1782-1788.

Li, R., Zou, X., Huang, H., Yu, Y., Zhang, H., Liu, P., Pan, S., Ouyang, Y., and Shang, Y. (2020a). HMGB1/PI3K/Akt/mTOR Signaling Participates in the Pathological Process of Acute Lung Injury by Regulating the Maturation and Function of Dendritic Cells. Frontiers in Immunology *11*.

Li, S.-W., Wang, C.-Y., Jou, Y.-J., Yang, T.-C., Huang, S.-H., Wan, L., Lin, Y.-J., and Lin, C.-W. (2016). SARS coronavirus papain-like protease induces Egr-1-dependent up-regulation of TGF-β1 via ROS/p38 MAPK/STAT3 pathway. Scientific Reports *6*, 25754.

Li, S., Liu, X., Chen, X., and Bi, L. (2020b). Research Progress on Anti-Inflammatory Effects and Mechanisms of Alkaloids from Chinese Medical Herbs. Evidence-Based Complementary and Alternative Medicine *2020*, 1303524.

Li, S.Y., Chen, C., Zhang, H.Q., Guo, H.Y., Wang, H., Wang, L., Zhang, X., Hua, S.N., Yu, J., Xiao, P.G.*, et al.* (2005). Identification of natural compounds with antiviral activities against SARS-associated coronavirus. Antiviral Res *67*, 18-23.

Li, X., Li, Y., Shan, L., Shen, E., Chen, R., and Peng, T. (2009). Over-expression of calpastatin inhibits calpain activation and attenuates myocardial dysfunction during endotoxaemia. Cardiovascular research *83*, 72-79.

Liu, J., Yang, Y., Xu, Y., Ma, C., Qin, C., and Zhang, L. (2011). Lycorine reduces mortality of human enterovirus 71-infected mice by inhibiting virus replication. Virology journal *8*, 483.

Liu, R., Qi, H., Wang, J., Wang, Y., Cui, L., Wen, Y., and Yin, C. (2014). Ulinastatin activates the renin-angiotensin system to ameliorate the pathophysiology of severe acute pancreatitis. Journal of gastroenterology and hepatology *29*, 1328-1337.

Ma, C., Sacco, M.D., Hurst, B., Townsend, J.A., Hu, Y., Szeto, T., Zhang, X., Tarbet, B., Marty, M.T., Chen, Y.*, et al.* (2020a). Boceprevir, GC-376, and calpain inhibitors II, XII inhibit SARS-CoV-2 viral replication by targeting the viral main protease. Cell research *30*, 678-692.

Ma, X., Yu, X., and Zhou, Q. (2020b). The IL1β-HER2-CLDN18/CLDN4 axis mediates lung barrier damage in ARDS. Aging (Albany NY) *12*, 3249-3265.

Madtes, D.K., Elston, A.L., Hackman, R.C., Dunn, A.R., and Clark, J.G. (1999). Transforming growth factor-alpha deficiency reduces pulmonary fibrosis in transgenic mice. American journal of respiratory cell and molecular biology *20*, 924-934.

Marois, I., Cloutier, A., Meunier, I., Weingartl, H.M., Cantin, A.M., and Richter, M.V. (2014). Inhibition of Influenza Virus Replication by Targeting Broad Host Cell Pathways. PLOS ONE *9*, e110631.

Mitchell, L.A., Overgaard, C.E., Ward, C., Margulies, S.S., and Koval, M. (2011). Differential effects of claudin-3 and claudin-4 on alveolar epithelial barrier function. American journal of physiology Lung cellular and molecular physiology *301*, L40-L49.

Mizutani, T., Fukushi, S., Saijo, M., Kurane, I., and Morikawa, S. (2004). Phosphorylation of p38 MAPK and its downstream targets in SARS coronavirus-infected cells. Biochem Biophys Res Commun *319*, 1228-1234.

Mugabe, B.E., Yaghini, F.A., Song, C.Y., Buharalioglu, C.K., Waters, C.M., and Malik, K.U. (2010). Angiotensin II-induced migration of vascular smooth muscle cells is mediated by p38 mitogen-activated protein kinase-activated c-Src through spleen tyrosine kinase and epidermal growth factor receptor transactivation. The Journal of pharmacology and experimental therapeutics *332*, 116-124.

Neveu, G., Barouch-Bentov, R., Ziv-Av, A., Gerber, D., Jacob, Y., and Einav, S. (2012). Identification and Targeting of an Interaction between a Tyrosine Motif within Hepatitis C Virus Core Protein and AP2M1 Essential for Viral Assembly. PLoS pathogens *8*, e1002845.

Novartis (2018). Tykerb (U.S. package insert).

O'Donovan, S.M., Imami, A., Eby, H., Henkel, N.D., Creeden, J.F., Asah, S., Zhang, X., Wu, X., Alnafisah, R., Taylor, R.T.*, et al.* (2021). Identification of candidate repurposable drugs to combat COVID-19 using a signature-based approach. Scientific Reports *11*, 4495.

Ohtsu, H., Dempsey, P.J., and Eguchi, S. (2006). ADAMs as mediators of EGF receptor transactivation by G protein-coupled receptors. Am J Physiol Cell Physiol *291*, C1-10.

Onishi, E., Natori, K., and Yamazaki, S. (1991). The antiviral effect of phorbol ester and calcium ionophore A23187 is not mediated by interferons. Journal of interferon research *11*, 171-175.

Oudit, G.Y., Kassiri, Z., Jiang, C., Liu, P.P., Poutanen, S.M., Penninger, J.M., and Butany, J. (2009). SARS-coronavirus modulation of myocardial ACE2 expression and inflammation in patients with SARS. European journal of clinical investigation *39*, 618-625.

Pan, H., Peto, R., Henao-Restrepo, A.M., Preziosi, M.P., Sathiyamoorthy, V., Abdool Karim, Q., Alejandria, M.M., Hernández García, C., Kieny, M.P., Malekzadeh, R.*, et al.* (2020). Repurposed Antiviral Drugs for Covid-19 - Interim WHO Solidarity Trial Results. The New England journal of medicine.

Perez, E.A., Koehler, M., Byrne, J., Preston, A.J., Rappold, E., and Ewer, M.S. (2008). Cardiac safety of lapatinib: pooled analysis of 3689 patients enrolled in clinical trials. Mayo Clinic proceedings *83*, 679-686.

Piccart-Gebhart, M., Holmes, E., Baselga, J., de Azambuja, E., Dueck, A.C., Viale, G., Zujewski, J.A., Goldhirsch, A., Armour, A., Pritchard, K.I.*, et al.* (2016). Adjuvant Lapatinib and Trastuzumab for Early Human Epidermal Growth Factor Receptor 2-Positive Breast Cancer: Results From the Randomized Phase III Adjuvant Lapatinib and/or Trastuzumab Treatment Optimization Trial. J Clin Oncol *34*, 1034-1042.

Pivot, X., Manikhas, A., Żurawski, B., Chmielowska, E., Karaszewska, B., Allerton, R., Chan, S., Fabi, A., Bidoli, P., Gori, S.*, et al.* (2015). CEREBEL (EGF111438): A Phase III, Randomized, Open-Label Study of Lapatinib Plus Capecitabine Versus Trastuzumab Plus Capecitabine in Patients With Human Epidermal Growth Factor Receptor 2-Positive Metastatic Breast Cancer. J Clin Oncol *33*, 1564-1573.

Pu, S., Schor, S., Karim, M., Saul, S., Robinson, M., Kumar, S., Prugar, L.I., Dorosky, D.E., Brannan, J., Dye, J.M.*, et al.* (2020). BIKE regulates dengue virus infection and is a cellular target for broad-spectrum antivirals. Antiviral Res *184*, 104966.

Qiu, C., Tarrant, M.K., Choi, S.H., Sathyamurthy, A., Bose, R., Banjade, S., Pal, A., Bornmann, W.G., Lemmon, M.A., Cole, P.A.*, et al.* (2008). Mechanism of activation and inhibition of the HER4/ErbB4 kinase. Structure (London, England : 1993) *16*, 460-467.

Rajapakse, A.G., Ming, X.F., Carvas, J.M., and Yang, Z. (2009). The hexosamine biosynthesis inhibitor azaserine prevents endothelial inflammation and dysfunction under hyperglycemic condition through antioxidant effects. American journal of physiology Heart and circulatory physiology *296*, H815-822.

Raymonda, M.H., Ciesla, J.H., Monaghan, M., Leach, J., Asantewaa, G., Smorodintsev-Schiller, L.A., Lutz, M.M., Schafer, X.L., Takimoto, T., Dewhurst, S.*, et al.* (2020). Pharmacologic profiling reveals lapatinib as a novel antiviral against SARS-CoV-2 in vitro. bioRxiv, 2020.2011.2025.398859.

Richardson, P., Griffin, I., Tucker, C., Smith, D., Oechsle, O., Phelan, A., and Stebbing, J. (2020). Baricitinib as potential treatment for 2019-nCoV acute respiratory disease. Lancet *395*, e30-e31.

Riva, L., Yuan, S., Yin, X., Martin-Sancho, L., Matsunaga, N., Pache, L., Burgstaller-Muehlbacher, S., De Jesus, P.D., Teriete, P., Hull, M.V.*, et al.* (2020). Discovery of SARS-CoV-2 antiviral drugs through large-scale compound repurposing. Nature *586*, 113-119.

Rusnak, D.W., Lackey, K., Affleck, K., Wood, E.R., Alligood, K.J., Rhodes, N., Keith, B.R., Murray, D.M., Knight, W.B., Mullin, R.J.*, et al.* (2001). The effects of the novel, reversible epidermal growth factor receptor/ErbB-2 tyrosine kinase inhibitor, GW2016, on the growth of human normal and tumor-derived cell lines in vitro and in vivo. Mol Cancer Ther *1*, 85-94.

Sahoo, M.K., Holubar, M., Huang, C., Mohamed-Hadley, A., Liu, Y., Waggoner, J.J., Troy, S.B., Garcia-Garcia, L., Ferreyra-Reyes, L., Maldonado, Y.*, et al.* (2017). Detection of Emerging Vaccine-Related Polioviruses by Deep Sequencing. Journal of clinical microbiology *55*, 2162-2171.

Sakurai, Y., Kolokoltsov, A.A., Chen, C.C., Tidwell, M.W., Bauta, W.E., Klugbauer, N., Grimm, C., Wahl-Schott, C., Biel, M., and Davey, R.A. (2015). Ebola virus. Two-pore channels control Ebola virus host cell entry and are drug targets for disease treatment. Science *347*, 995-998.

Sasaki, T., Kishi, M., Saito, M., Tanaka, T., Higuchi, N., Kominami, E., Katunuma, N., and Murachi, T. (1990). Inhibitory effect of di- and tripeptidyl aldehydes on calpains and cathepsins. Journal of enzyme inhibition *3*, 195-201.

Saul, S., and Einav, S. (2020). Old Drugs for a New Virus: Repurposed Approaches for Combating COVID-19. ACS infectious diseases.

Schneider, M., Ackermann, K., Stuart, M., Wex, C., Protzer, U., Schätzl, H.M., and Gilch, S. (2012). Severe acute respiratory syndrome coronavirus replication is severely impaired by MG132 due to proteasome-independent inhibition of M-calpain. J Virol *86*, 10112-10122.

Schwartzberg, L.S., Franco, S.X., Florance, A., O'Rourke, L., Maltzman, J., and Johnston, S. (2010). Lapatinib plus letrozole as first-line therapy for HER-2+ hormone receptor-positive metastatic breast cancer. The oncologist *15*, 122-129.

Selvaraj, G., Kaliamurthi, S., Peslherbe, G., and Wei, D. (2021). Identifying potential drug targets and candidate drugs for COVID-19: biological networks and structural modeling approaches [version 1; peer review: 1 approved with reservations]. F1000Research *10*.

Simões e Silva, A.C., Silveira, K.D., Ferreira, A.J., and Teixeira, M.M. (2013). ACE2, angiotensin-(1-7) and Mas receptor axis in inflammation and fibrosis. Br J Pharmacol *169*, 477-492.

Sokol, C.L., and Luster, A.D. (2015). The chemokine system in innate immunity. Cold Spring Harbor perspectives in biology *7*.

Spagnolo, P., Balestro, E., Aliberti, S., Cocconcelli, E., Biondini, D., Casa, G.D., Sverzellati, N., and Maher, T.M. (2020). Pulmonary fibrosis secondary to COVID-19: a call to arms? The Lancet Respiratory medicine *8*, 750-752.

Spinner, C.D., Gottlieb, R.L., Criner, G.J., Arribas López, J.R., Cattelan, A.M., Soriano Viladomiu, A., Ogbuagu, O., Malhotra, P., Mullane, K.M., Castagna, A.*, et al.* (2020). Effect of Remdesivir vs Standard Care on Clinical Status at 11 Days in Patients With Moderate COVID-19: A Randomized Clinical Trial. Jama.

Spiteri, G., Fielding, J., Diercke, M., Campese, C., Enouf, V., Gaymard, A., Bella, A., Sognamiglio, P., Sierra Moros, M.J., Riutort, A.N.*, et al.* (2020). First cases of coronavirus disease 2019 (COVID-19) in the WHO European Region, 24 January to 21 February 2020. Euro Surveill *25*.

Sugamata, R., Sugawara, A., Nagao, T., Suzuki, K., Hirose, T., Yamamoto, K., Oshima, M., Kobayashi, K., Sunazuka, T., Akagawa, K.S.*, et al.* (2014). Leucomycin A3, a 16-membered macrolide antibiotic, inhibits influenza A virus infection and disease progression. The Journal of antibiotics *67*, 213-222.

Sun, C., Gardner, C.L., Watson, A.M., Ryman, K.D., and Klimstra, W.B. (2014). Stable, high-level expression of reporter proteins from improved alphavirus expression vectors to track replication and dissemination during encephalitic and arthritogenic disease. Journal of virology *88*, 2035-2046.

Supinski, G.S., and Callahan, L.A. (2010). Calpain activation contributes to endotoxin-induced diaphragmatic dysfunction. American journal of respiratory cell and molecular biology *42*, 80-87.

Sutton, P., Borgia, J.A., Bonomi, P., and Plate, J.M. (2013). Lyn, a Src family kinase, regulates activation of epidermal growth factor receptors in lung adenocarcinoma cells. Mol Cancer *12*, 76.

Szlávik, L., Gyuris, A., Minárovits, J., Forgo, P., Molnár, J., and Hohmann, J. (2004). Alkaloids from Leucojum vernum and antiretroviral activity of Amaryllidaceae alkaloids. Planta medica *70*, 871-873.

Tabara, H., Naito, Y., Ito, A., Katsuma, A., Sakurai, M.A., Ohno, S., Shimizu, H., Yabuta, N., and Nojima, H. (2011). Neonatal lethality in knockout mice expressing the kinase-dead form of the gefitinib target GAK is caused by pulmonary dysfunction. PLoS One *6*, e26034.

Tang, H., Nishishita, T., Fitzgerald, T., Landon, E.J., and Inagami, T. (2000). Inhibition of AT1 receptor internalization by concanavalin A blocks angiotensin II-induced ERK activation in vascular smooth muscle cells. Involvement of epidermal growth factor receptor proteolysis but not AT1 receptor internalization. The Journal of biological chemistry *275*, 13420-13426.

Teranishi, F., Liu, Z.Q., Kunimatsu, M., Imai, K., Takeyama, H., Manabe, T., Sasaki, M., and Okamoto, T. (2003). Calpain is involved in the HIV replication from the latently infected OM10.1 cells. Biochem Biophys Res Commun *303*, 940-946.

Tindle, C., Fuller, M., Fonseca, A., Taheri, S., Ibeawuchi, S.R., Beutler, N., Claire, A., Castillo, V., Hernandez, M., Russo, H.*, et al.* (2020). Adult Stem Cell-derived Complete Lung Organoid Models Emulate Lung Disease in COVID-19. bioRxiv.

Toi, M., Iwata, H., Fujiwara, Y., Ito, Y., Nakamura, S., Tokuda, Y., Taguchi, T., Rai, Y., Aogi, K., Arai, T.*, et al.* (2009). Lapatinib monotherapy in patients with relapsed, advanced, or metastatic

breast cancer: efficacy, safety, and biomarker results from Japanese patients phase II studies. British journal of cancer *101*, 1676-1682.

Torrisi, J.M., Schwartz, L.H., Gollub, M.J., Ginsberg, M.S., Bosl, G.J., and Hricak, H. (2011). CT findings of chemotherapy-induced toxicity: what radiologists need to know about the clinical and radiologic manifestations of chemotherapy toxicity. Radiology *258*, 41-56.

Treon, S.P., Castillo, J.J., Skarbnik, A.P., Soumerai, J.D., Ghobrial, I.M., Guerrera, M.L., Meid, K., and Yang, G. (2020). The BTK inhibitor ibrutinib may protect against pulmonary injury in COVID-19-infected patients. Blood *135*, 1912-1915.

Upla, P., Marjomäki, V., Nissinen, L., Nylund, C., Waris, M., Hyypiä, T., and Heino, J. (2008). Calpain 1 and 2 are required for RNA replication of echovirus 1. J Virol *82*, 1581-1590.

Venkataraman, T., Coleman, C.M., and Frieman, M.B. (2017). Overactive Epidermal Growth Factor Receptor Signaling Leads to Increased Fibrosis after Severe Acute Respiratory Syndrome Coronavirus Infection. Journal of virology *91*, e00182-00117.

Vrijsen, R., Vanden Berghe, D.A., Vlietinck, A.J., and Boeyé, A. (1986). Lycorine: a eukaryotic termination inhibitor? The Journal of biological chemistry *261*, 505-507.

Wang, P.-G., Tang, D.-J., Hua, Z., Wang, Z., and An, J. (2020a). Sunitinib reduces the infection of SARS-CoV, MERS-CoV and SARS-CoV-2 partially by inhibiting AP2M1 phosphorylation. Cell Discovery *6*, 71.

Wang, Y., Zhang, D., Du, G., Du, R., Zhao, J., Jin, Y., Fu, S., Gao, L., Cheng, Z., Lu, Q*., et al.* (2020b). Remdesivir in adults with severe COVID-19: a randomised, double-blind, placebo-controlled, multicentre trial. Lancet *395*, 1569-1578.

World Health, O. (2020). Clinical management of COVID-19: interim guidance, 27 May 2020 (Geneva: World Health Organization).

Wu, Z., and McGoogan, J.M. (2020). Characteristics of and Important Lessons From the Coronavirus Disease 2019 (COVID-19) Outbreak in China: Summary of a Report of 72 314 Cases From the Chinese Center for Disease Control and Prevention. JAMA *323*, 1239-1242.

Xu, B.-H., Jiang, Z.-F., Chua, D., Shao, Z.-M., Luo, R.-C., Wang, X.-J., Liu, D.-G., Yeo, W., Yu, S.-Y., Newstat, B.*, et al.* (2011). Lapatinib plus capecitabine in treating HER2-positive advanced breast cancer: efficacy, safety, and biomarker results from Chinese patients. Chin J Cancer *30*, 327-335.

Yang, L., Zhang, J.H., Zhang, X.L., Lao, G.J., Su, G.M., Wang, L., Li, Y.L., Ye, W.C., and He, J. (2019). Tandem mass tag-based quantitative proteomic analysis of lycorine treatment in highly pathogenic avian influenza H5N1 virus infection. PeerJ *7*, e7697-e7697.

Zarubin, T., and Han, J. (2005). Activation and signaling of the p38 MAP kinase pathway. Cell research *15*, 11-18.

Zhang, X.L., Xing, R.G., Chen, L., Liu, C.R., and Miao, Z.G. (2016). PI3K/Akt signaling is involved in the pathogenesis of bleomycin-induced pulmonary fibrosis via regulation of epithelial-mesenchymal transition. Molecular medicine reports *14*, 5699-5706.

Zheng, K., Xiang, Y., Wang, Q., Jin, F., Chen, M., Ma, K., Ren, Z., and Wang, Y. (2014). Calcium-signal facilitates herpes simplex virus type 1 nuclear transport through slingshot 1 and calpain-1 activation. Virus research *188*, 32-37.

Zhou, Y., Lee, J.-Y., Lee, C.-M., Cho, W.-K., Kang, M.-J., Koff, J.L., Yoon, P.-O., Chae, J., Park, H.-O., Elias, J.A.*, et al.* (2012). Amphiregulin, an epidermal growth factor receptor ligand, plays an essential role in the pathogenesis of transforming growth factor-β-induced pulmonary fibrosis. The Journal of biological chemistry *287*, 41991-42000.

Zoeller, R.A., and Geoghegan-Barek, K. (2019). A cell-based high-throughput screen identifies tyrphostin AG 879 as an inhibitor of animal cell phospholipid and fatty acid biosynthesis. Biochemistry and Biophysics Reports *18*, 100621.

Zona, L., Lupberger, J., Sidahmed-Adrar, N., Thumann, C., Harris, Helen J., Barnes, A., Florentin, J., Tawar, Rajiv G., Xiao, F., Turek, M.*, et al.* (2013). HRas Signal Transduction Promotes Hepatitis C Virus Cell Entry by Triggering Assembly of the Host Tetraspanin Receptor Complex. Cell Host & Microbe *13*, 302-313.

Zou, G., Xu, H.Y., Qing, M., Wang, Q.-Y., and Shi, P.-Y. (2011). Development and characterization of a stable luciferase dengue virus for high-throughput screening. Antiviral research *91*, 11-19.

Figures and legends:

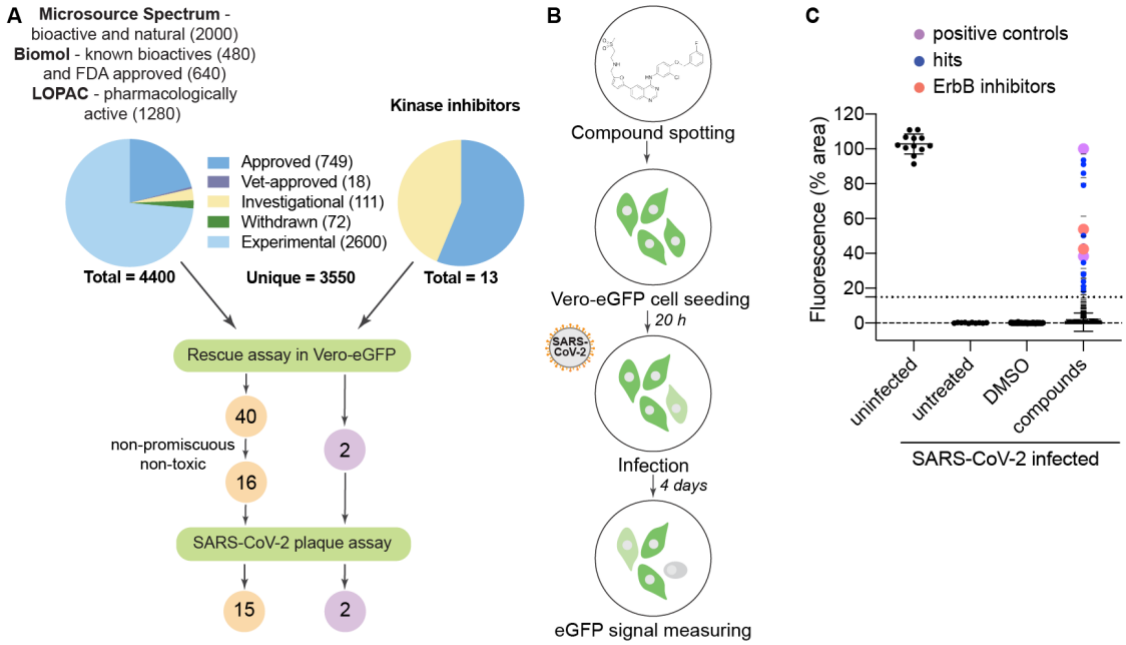

D

	SARS-CoV-2			
	EC_{50}	CC_{50}	SI	
Ac-Leu-Leu-Nle-CHO	0.2	>20	>100	
Aurothioglucose	0.4	>20	>50	
Lapatinib	0.5	>20	>40	#
Lycorine	0.5	>20	>40	
Calcimycin	0.6	>20	>33	
Tyrphostin AG 879	0.6	>20	>33	
Azaserine	0.7	>20	>29	
Monensin	1.2	>20	>17	
Gedunin	1.4	>20	>14	
Tetrandrine	1.4	>20	>14	
Josamycin	2.4	>20	>8.3	
Sunitinib	2.4	12	5.1	#
Spiperone	4.3	>20	>4.7	
Fluspirilene	15	>20	>1.3	
Loperamide	16	>20	>1.2	
Tyrphostin A9	17	>20	>1.2	
Penitrem A	18	>20	>1.1	
Salbutamol	>20	>20	>1	

+ EC_{50} - activity

+ CC_{50} - toxicity

E

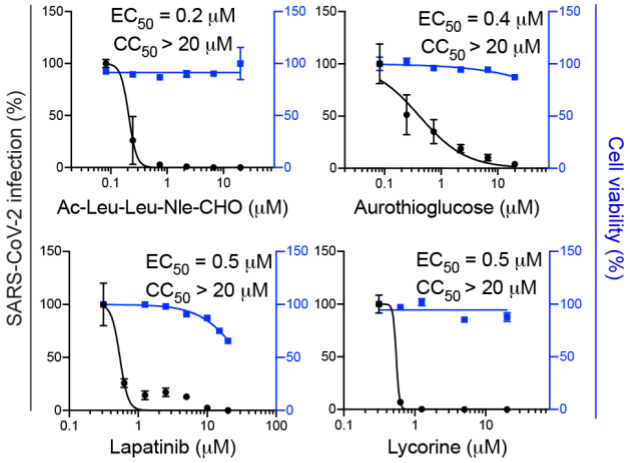

F

Class	Compound	Status
RTK inhibitors with anti-ErbB activity	Lapatinib	Approved (cancer)
	Tyrphostin AG 879	Experimental
Kinase inhibitor with anti-NAK activity	Sunitinib	Approved (cancer)
Compounds targeting ion transport	Tetrandrine	Natural product
	Calcimycin	Investigational
	Monensin	Natural product
HSP90 inhibitor	Gedunin	Natural product
Cysteine protease inhibitor	Ac-Leu-Leu-Nle-CHO	Experimental
Glutamine amidotransferase inhibitor	Azaserine	Natural product
Phagocytosis inhibitor	Aurothioglucose	Natural product, approved (RA)
Protein synthesis inhibitor	Lycorine	Natural product
Macrolide antibiotic	Josamycin	Natural product, approved

Figure 1. High-throughput screening (HTS) for compounds that counteract SARS-CoV-2-induced lethality and validation by plaque assays.

(A) Schematic of the screening and hit selection pipeline and the composition of the screened libraries.

(B) HTS assay schematic. Compounds were pre-spotted in 384-well plates at a final concentration of 10 μM. Next, Vero E6 cells constitutively expressing eGFP were added to each well and pre-incubated for 20 hours with the compounds, followed by SARS-CoV-2 infection (Belgium-GHB-03021, MOI = 0.001). eGFP signal measured at 4 days post-infection was used as an indicator for survival from viral-induced lethality.

(C) Boxplots of the percentage of fluorescence area values combining the entire HTS data set (two independent experiments) split into the four indicated categories. The box horizontal lines indicate the first, second (median), and third quartiles. Outliers above a cutoff of 15% were defined as positive hits. Dots represent individual compounds and colors denote positive controls (purple), new hits (blue), and ErbB inhibitors (peach).

(D) Heat map of the EC_{50} and CC_{50} values of hits emerging in the HTS color-coded based on the antiviral activity measured by plaque assays (green) and toxicity measured by alamarBlue assays (peach) 24 hours post-infection of Vero cells with SARS-CoV-2 (USA-WA1/2020 strain; MOI=0.05). Selectivity indices (SI) greater than 5 are depicted in yellow. # indicates compounds from the 13-kinase set that also protect from SARS-CoV-2 lethality in the HTS.

(E) Representative dose-response curves of hits depicting SARS-CoV-2 infection (black) and cell viability (blue). Data are relative to DMSO.

(F) The 12 most promising hit compounds emerging in the HTS.

Data in panels D, E are representative of 2 or more independent experiments. Individual experiments had 3 biological replicates. Shown are means ± SD. RA, Rheumatoid arthritis; RTK, receptor tyrosine kinase; NAK, NUMB-associated kinase.

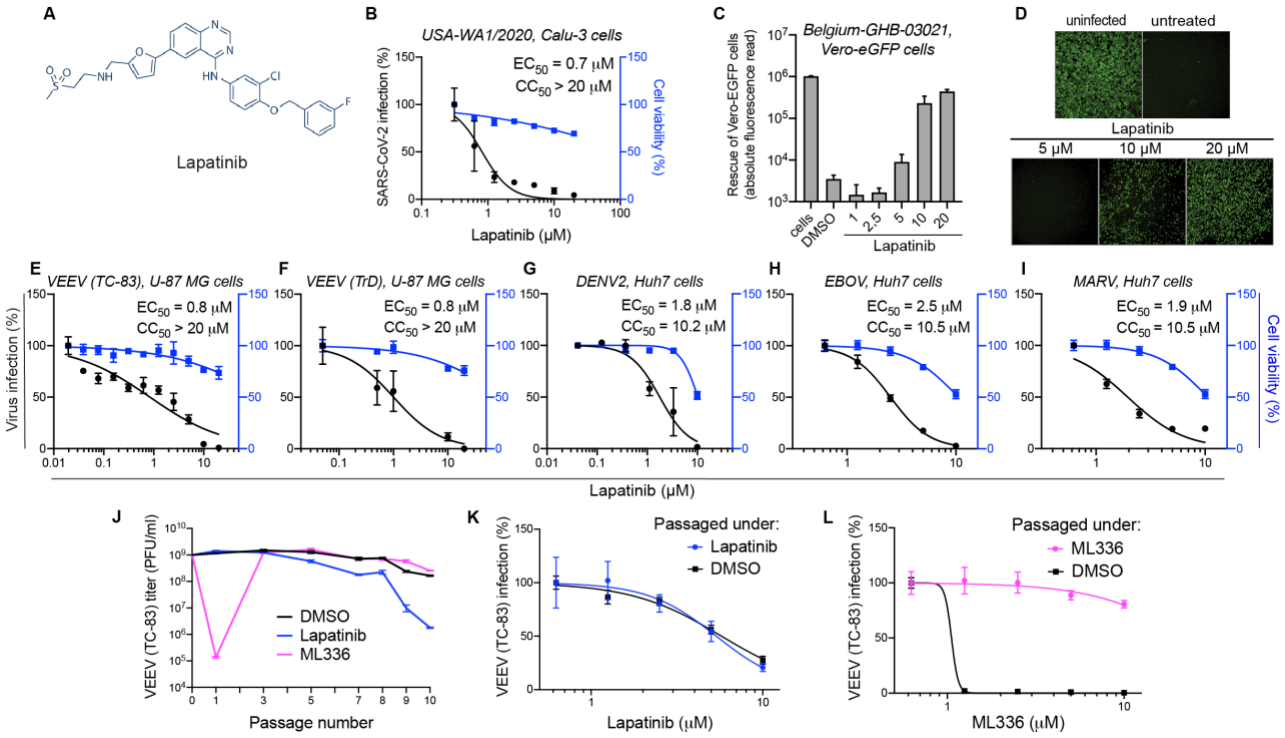

Figure 2, Lapatinib is a potent broad-spectrum antiviral with a high genetic barrier to resistance.

(A) Chemical structure of lapatinib. (B) Dose response to lapatinib of SARS-CoV-2 infection (black, USA-WA1/2020 strain; MOI=0.05) and cell viability (blue) in Calu-3 cells via plaque and alamarBlue assays at 24 hours post-infection, respectively. (C, D) Dose-dependent graph (C) and corresponding florescence images (D) of Vero-eGFP cells rescued from SARS-CoV-2-induced lethality by lapatinib at 96 hours post-infection (Belgium-GHB-03021 strain; MOI=0.05). (E, F) Dose response to lapatinib of infection with vaccine (TC-83) (E) and WT (Trinidad donkey (TrD)) (F) VEEV strains (MOI=0.1) in U-87 MG cells via plaque and alamarBlue assays at 24 hours post-infection, respectively. (G) Dose response of DENV2 infection (blue) and cellular viability (black) to lapatinib measured in Huh7 cells via plaque and alamarBlue assays at 24 hours post-infection (MOI=0.1), respectively. (H, I) Dose response of EBOV (Kikwit isolate, MOI=1) (H) and MARV (Ci67 strain, MOI=2) (I) infections (blue) and cellular viability (black) to lapatinib measured in Huh7 cells 48 hours post-infection via microneutralization assay and CellTiter-Glo luminescent cell viability assay, respectively.(J) VEEV (TC-83) was used to infect U-87 MG cells (MOI=0.1) and was then passaged every 24 hours by inoculation of naive U-87 MG cells with equal volumes of viral supernatants under DMSO treatment or selection with lapatinib or ML336 (VEEV nsP2 inhibitor) increasing from 2.5 to 15 μM over 10 passages. Viral titers were measured by plaque assays. (K, L) Dose response to lapatinib (K) and ML336 (L) of VEEV (TC-83) harvested after 10 passages in U-87 MG cells in the presence of lapatinib (K) and ML336 (L), via luciferase assays. Data are representative of at least 2 experiments. All panels except J had 2 and 3 biological replicates. Means ± SD are shown. Data in B, E-I, K and L are relative to DMSO.

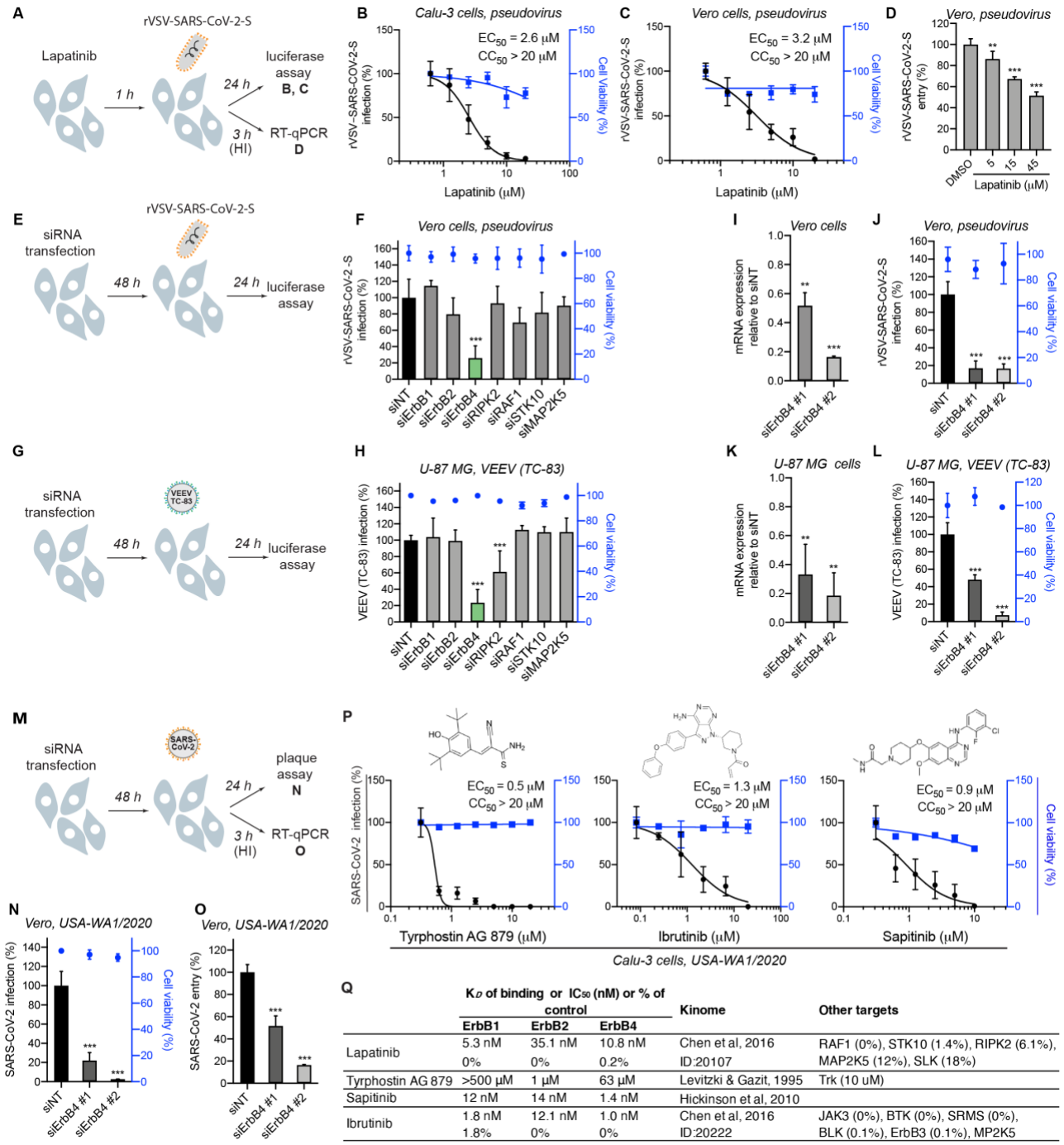

Q

	K_D of binding or IC_{50} (nM) or % of control			Kinome	Other targets
	ErbB1	ErbB2	ErbB4		
Lapatinib	5.3 nM 0%	35.1 nM 0%	10.8 nM 0.2%	Chen et al, 2016 ID:20107	RAF1 (0%), STK10 (1.4%), RIPK2 (6.1%), MAP2K5 (12%), SLK (18%)
Tyrphostin AG 879	>500 μM	1 μM	63 μM	Levitzki & Gazit, 1995	Trk (10 uM)
Sapitinib	12 nM	14 nM	1.4 nM	Hickinson et al, 2010	
Ibrutinib	1.8 nM 1.8%	12.1 nM 0%	1.0 nM 0%	Chen et al, 2016 ID:20222	JAK3 (0%), BTK (0%), SRMS (0%), BLK (0.1%), ErbB3 (0.1%), MP2K5

Figure 3. ErbB4, but not other lapatinib's targets, is essential for SARS-CoV-2 entry and VEEV (TC-83) infection.

(A) Schematic of the experiments shown in panels B-D.

(B-C) Dose response to lapatinib of rVSV-SARS-CoV-2-S infection (black) and cell viability (blue) in Calu-3 (B) and Vero (C) cells via luciferase and alamarBlue assays at 24 hours post-infection with a standard inoculum, respectively.

(D) Dose response to lapatinib of rVSV-SARS-CoV-2-S entry in Vero cells by RT-qPCR at 3 hours post-infection with a high inoculum (HI).

(E) Schematic of the experiments shown in panels F, I, J.

(F) rVSV-SARS-CoV-2-S infection by luciferase assays and cell viability by alamarBlue assays (blue) measured at 24 hours post-infection of Vero cells transfected with the indicated siRNA pools.

(G) Schematic of the experiments shown in panels H, K, L.

(H) VEEV (T-83) infection by luciferase assays and cell viability by alamarBlue assays (blue) measured at 24 hours post-infection of U-87 MG cells transfected with the indicated siRNA pools (MOI=0.1).

(I, K) Confirmation of gene expression knockdown by RT-qPCR in Vero (I) and U-87 MG (K) cells at 48 hours post-transfection.

(J, L) rVSV-SARS-CoV-2-S (J) and VEEV (T-83) infection (MOI=0.1) (L) measured by luciferase assays at 24 hours post-infection of Vero or U-87 MG cells transfected with the indicated siRNAs, respectively. Shown in blue is cell viability by alamarBlue assays.

(M) Schematic of the experiments shown in panels N and O.

(N) SARS-CoV-2 infection at 24 hours post-infection of ErbB4-depleted Vero cells with SARS-CoV-2 (USA-WA1/2020 strain; MOI=0.05) by plaque assays.

(O) SARS-CoV-2 entry at 3 hours post-infection of Vero cells (MOI=1) by RT-qPCR.

(P) Chemical structures and dose response to tyrphostin AG 879, ibrutinib and sapitinib of SARS-CoV-2 infection (black, USA-WA1/2020 strain; MOI=0.05) by plaque assays and cell viability (blue) by alamarBlue assays at 24 hours post-infection of Calu-3 cells.

(Q) Binding affinity (K_D), enzymatic activity (IC_{50}) or percent binding of control (% control) of the indicated kinase inhibitors on the 3 catalytic ErbBs, the source of kinome data, and other targets these compounds bind and/or inhibit.

Data in all panels are representative of 2 or more independent experiments. Individual experiments had 3 biological replicates, means ± SD are shown. *$P < 0.05$, **$P < 0.01$, ***$P < 0.001$ relative to DMSO (B-D, P) or to siNT (F-O) (one-way ANOVA followed by Dunnett's multiple comparisons test).

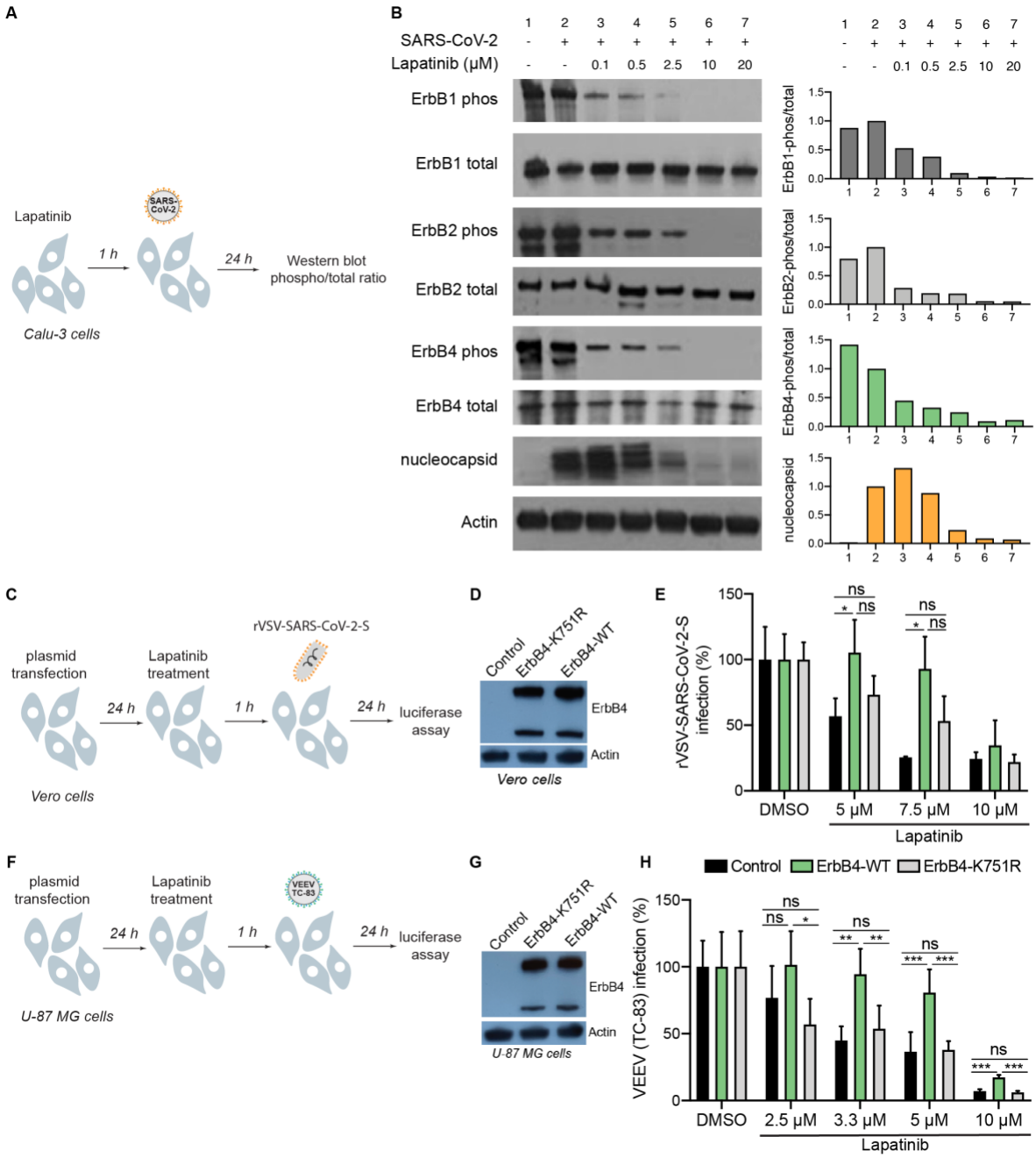

Figure 4. Lapatinib's antiviral activity is correlated with functional inhibition of ErbB activity and is mediated by ErbB4.

(A) Schematic of the experiment shown in B.

(B) ErbB1, 2 and 4 phosphorylation in Calu-3 cells that are uninfected (lane 1), infected and treated with DMSO (lane 2) or infected and treated with increasing concentrations of lapatinib (lanes 3-7) measured by Western blotting 24 hours post-infection with SARS-CoV-2 (USA-WA1/2020 strain, MOI=1). Shown are representative membranes blotted for phospho- and total

ErbB1, 2, and 4, SARS-CoV-2 nucleocapsid and actin and quantitative phospho- to total protein ratio data relative to infected cells treated with DMSO.

(C, F) Schematics of the experiments shown in D, E (C) and G, H (F).

(D, G) Level of ErbB4 and actin expression measured by Western blot following transfection of Vero (D) or U-87 MG (G) cells with control or ErbB4-expressing plasmids.

(E, H) Rescue of rVSV-SARS-CoV-2-S infection (E) or VEEV (TC-83) infection (H) in the presence of lapatinib upon ectopic expression of the indicated plasmids measured by luciferase assays 24 hours after infection in Vero (E) or U-87 MG cells (H).

Data in all panels are representative of 2 or more independent experiments. Shown in panels E and H are means±SD of results of two combined experiments conducted each with three (E) or five (H) replicates. *$P < 0.05$, **$P < 0.01$ **,** ***$P < 0.001$ relative to DMSO by 1-way ANOVA with Tukey's multiple comparisons test at each lapatinib concentration. Ns, non-significant.

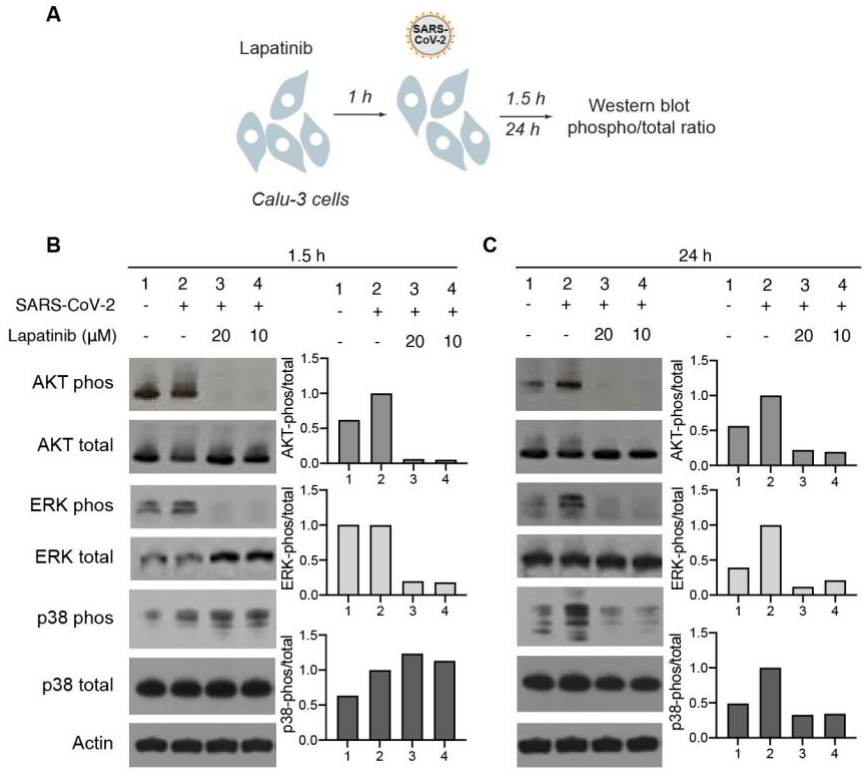

Figure 5. Lapatinib inhibits SARS-CoV-2-induced activation of ErbB-regulated inflammatory and tissue injury signals,

(A) Schematic of the experiment shown in B.

(B) AKT, ERK, and p38 MAPK phosphorylation in Calu-3 cells that are uninfected (lane 1), infected and treated with DMSO (lane 2) or infected and treated with lapatinib (lanes 3 and 4) measured by Western blotting 1.5 hours (B) and 24 hours (C) post-infection with SARS-CoV-2 (USA-WA1/2020 strain, MOI=1). Shown are representative membranes blotted for actin and phospho- and total AKT, ERK, and p38 MAPK and quantitative phospho- to total protein ratio data relative to infected cells treated with DMSO (lane 2).

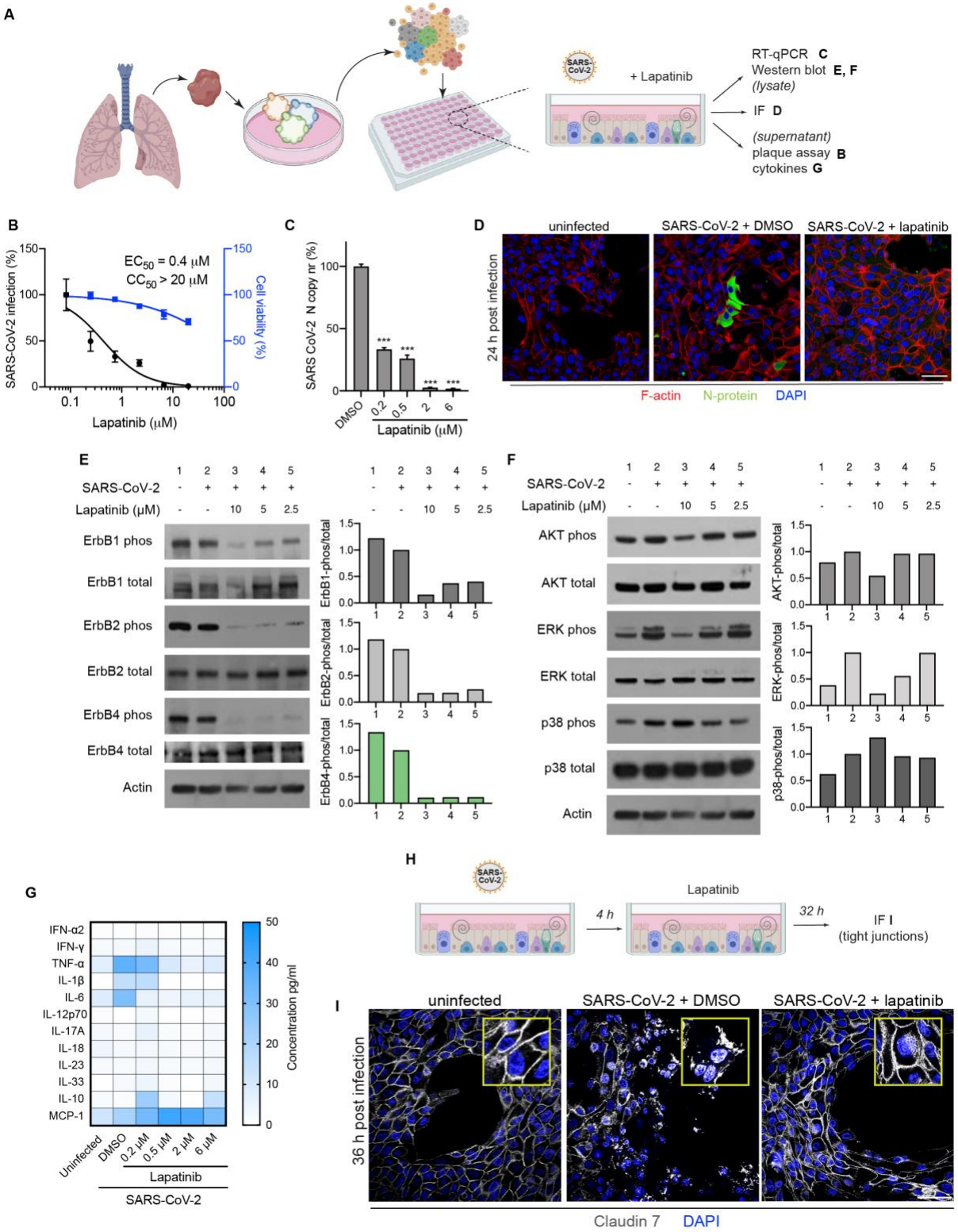
A
SARS-CoV-2
+ Lapatinib
RT-qPCR C
Western blot E, F
(lysate)
IF D
(supernatant)
plaque assay B
cytokines G
B
EC50 = 0.4 μM
CC50 > 20 μM
SARS-CoV-2 infection (%)
Cell viability (%)
Lapatinib (μM)
C
SARS CoV-2 N copy nr (%)
DMSO
0.2
0.5
2
6
Lapatinib (μM)
D
uninfected
SARS-CoV-2 + DMSO
SARS-CoV-2 + lapatinib
24 h post infection
F-actin
N-protein
DAPI
E
SARS-CoV-2
Lapatinib (μM)
ErbB1 phos
ErbB1 total
ErbB2 phos
ErbB2 total
ErbB4 phos
ErbB4 total
Actin
ErbB1-phos/total
ErbB2-phos/total
ErbB4-phos/total
F
AKT phos
AKT total
ERK phos
ERK total
p38 phos
p38 total
Actin
AKT-phos/total
ERK-phos/total
p38-phos/total
G
IFN-α2
IFN-γ
TNF-α
IL-1β
IL-6
IL-12p70
IL-17A
IL-18
IL-23
IL-33
IL-10
MCP-1
Concentration pg/ml
Uninfected
DMSO
0.2 μM
0.5 μM
2 μM
6 μM
Lapatinib
SARS-CoV-2
H
SARS-CoV-2
Lapatinib
4 h
32 h
IF I
(tight junctions)
I
uninfected
SARS-CoV-2 + DMSO
SARS-CoV-2 + lapatinib
36 h post infection
Claudin 7
DAPI

Figure 6. Lapatinib inhibits SARS-CoV-2 infection, inflammation, and tissue injury *ex vivo* in human adult lung organoids (ALOs).

(A) Schematic of the ALO model and the experimental procedures. ALOs were infected with virulent SARS-CoV-2 (USA-WA1/2020 strain, MOI=1).

(B) Dose response to lapatinib of SARS-CoV-2 infection (black) and cell viability (blue) in ALO supernatants via plaque and alamarBlue assays at 48 hours post-infection, respectively.

(C) Dose response to lapatinib of SARS-CoV-2 nucleocapsid (N) copy number in ALO lysates by RT-qPCR assays at 48 hours post-infection.

(D) Confocal IF microscopy images of F-actin (red), SARS-CoV-2 nucleocapsid (green) and DAPI (blue) in naïve and SARS-CoV-2-infected ALOs pre-treated with DMSO or 10 µM lapatinib 24 hours post-infection.

(E, F) Dose-dependent effect of lapatinib treatment on ErbB1, 2 and 4 (E) and AKT, ERK and p38 MAPK (F) phosphorylation in ALOs that are uninfected (lane 1), SARS-CoV-2-infected and treated with DMSO (lane 2) or infected and treated with lapatinib (lanes 3-5) measured by Western blotting 48 hours post-infection. Shown are representative membranes blotted for phospho- and total kinases and actin and quantitative phospho- to total kinase ratio data relative to infected ALOs treated with DMSO (lane 2).

(G) Heat map showing the concentration of cytokines (pg/mL) in the supernatants of ALOs under the indicated conditions at 48 hours post-infection with SARS-CoV-2 measured by LEGENDplex (Biolegend) kit.

(H) Schematic of the experiment shown in I.

(I) Confocal IF microscopy images of Claudin 7 (gray) and DAPI (blue) in naïve or SARS-CoV-2-infected ALOs treated at 4 hours post-infection either with DMSO or 10 µM lapatinib and imaged at 36 hours post-infection.

Data in all panels are representative of 2 or more independent experiments.

Individual experiments had 3 biological replicates, means ± SD are shown in panels B and C.

Representative merged images at 40x magnification are shown in panels D and I. Scale bars are 50 µm. $^{*}P < 0.05$, $^{**}P < 0.01$, $^{***}P < 0.001$ relative to DMSO (C) (one-way ANOVA followed by Dunnett's multiple comparisons test).

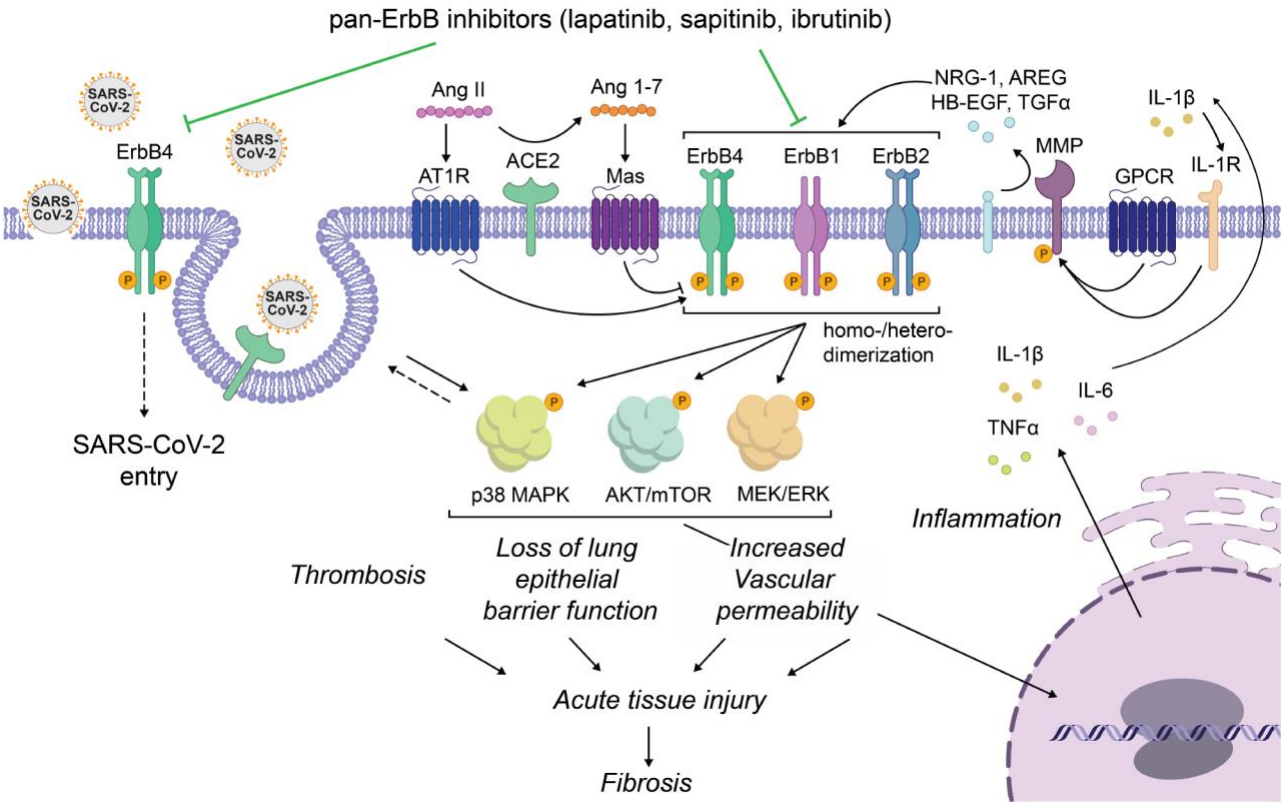

Figure 7. Proposed model for the roles of ErbBs in the regulation of SARS-CoV-2 infection and pathogenesis and the mechanism of action of pan-ErbB inhibitors. By inhibiting ErbB4, lapatinib suppresses SARS-CoV-2 entry. By inhibiting pan-ErbB activation by various ligands and unopposed Ang II effect, lapatinib inhibits activation of signaling pathways known to be activated and deleterious in severe pandemic coronaviral infections, thereby protecting from inflammation and tissue injury.

Supplemental Items

Figure S1. Related to Figure 1.
Characteristics of the HTS

Figure S2. Related to Figure 1.
Broad-spectrum potential of hits and kinase inhibitor set

Figure S3. Related to Figure 3.
Validation of ErbB4 as an antiviral target.

Figure S4. Related to Figure 4.
ErbB4 is modulated by lapatinib and is the molecular target mediating its antiviral effect.

Figure S5. Related to Figure 6.
Human ALOs for studying the antiviral and tissue protective effects of lapatinib.

A

Kinase inhibitors	Status
Baricitinib	Approved (RA)
Erlotinib	Approved (cancer)
Gefitinib	Approved (cancer)
Lapatinib	Approved (cancer)
Ribociclib	Approved (cancer)
Selumetinib	Approved (NF1)
Sunitinib	Approved (cancer)
Trametinib	Approved (cancer)
Vandetanib	Approved (cancer)
Dinaciclib	Investigational (phase 3)
Sapitinib	Investigational (phase 2)
Saracatinib	Investigational (phase 2)
Tesevatinib	Investigational (phase 2)

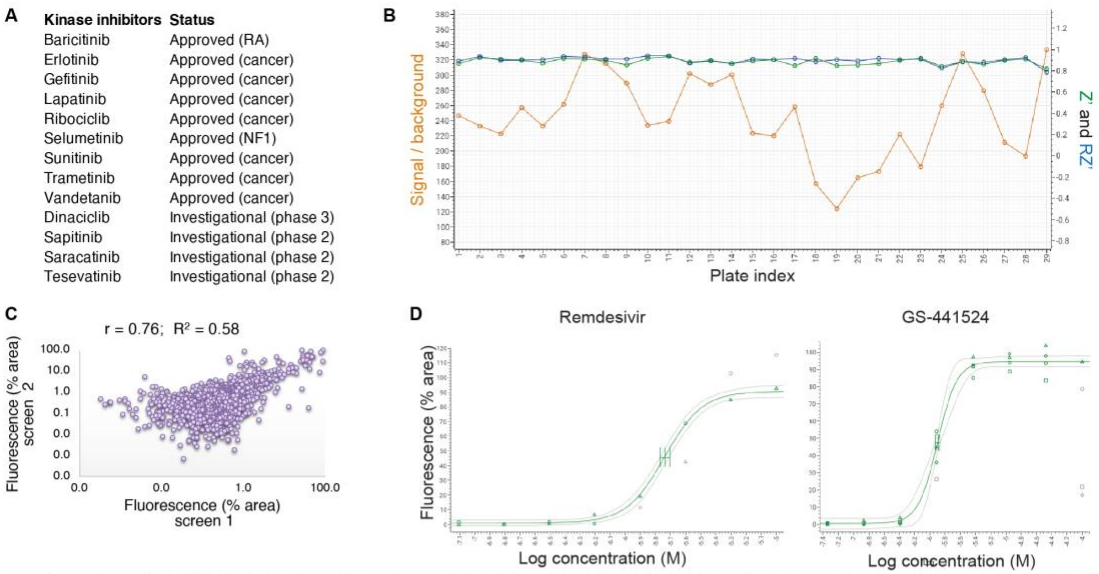

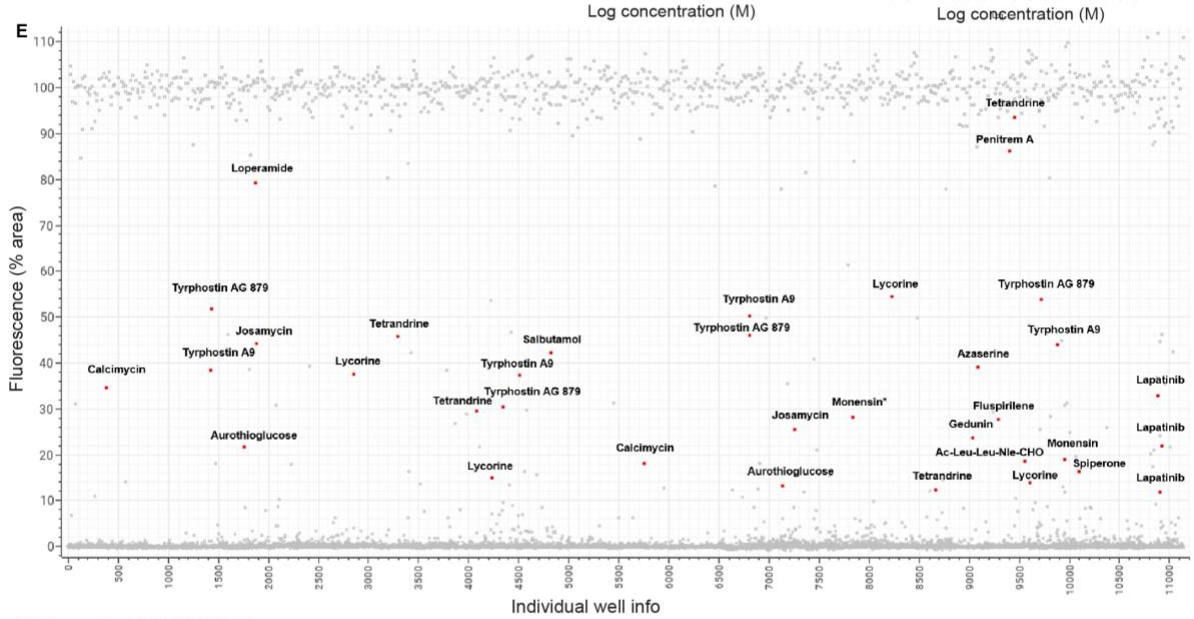

F *Vero cells, USA-WA1/2020*

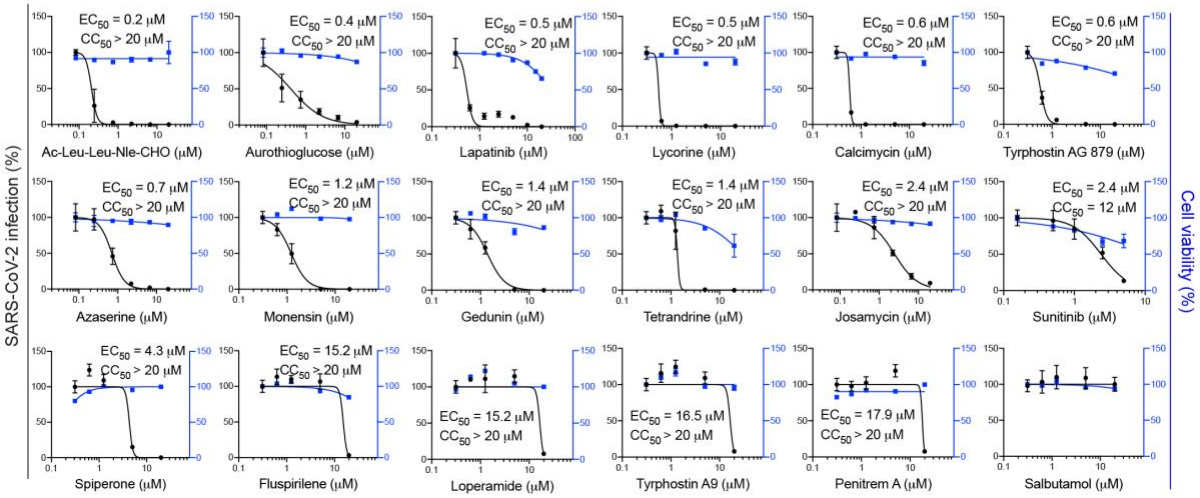

1686

Figure S1. Related to Figure 1.

Characteristics of the HTS.

(A) The kinase inhibitors included in the self-assembled set.

(B) Quality control of each individual plate of the 29 screened by determination of the signal-to-background (S/B), and the Z' and RZ' values. All three parameters were measured for each 384-well screening plate using the virus control (infected, DMSO treated) and cell control (uninfected, untreated) wells. S/B values ranged from 124 – 333. Z' and RZ' values were > 0.78. Generally, S/B values >10 and (R)Z' values >0,5 are accepted as qualitative assays. All parameters were calculated using Genedata Screener.

(C) Scatter plot of the two replicate screens with a Pearson's correlation coefficient (*r*) of 0.76.

(D) Dose-dependent rescue of Vero-eGFP cells from SARS-CoV-2-induced lethality by remdesivir and its major metabolite, GS-441524, used as positive controls, 4 days post-infection with SARS-CoV-2 (Belgium-GHB-03021, MOI=0.001)

(E) Percentage of fluorescence area values from all wells including the virus controls (infected, DMSO treated) and the cell controls (uninfected, untreated) from the 29 384-well plates. The red dots depict hits emerging in the screening. Grey dots represent reference compounds such as nelfinavir, GS-441524 and compounds not prioritized for further analysis.

(F) Dose-dependent to the indicated hits emerging from the HTS of SARS-CoV-2 infection (black, USA-WA1/2020 strain, MOI=0.05) and cell viability (blue) in Vero cells via plaque and alamarBlue assays at 24 hours post-infection, respectively.

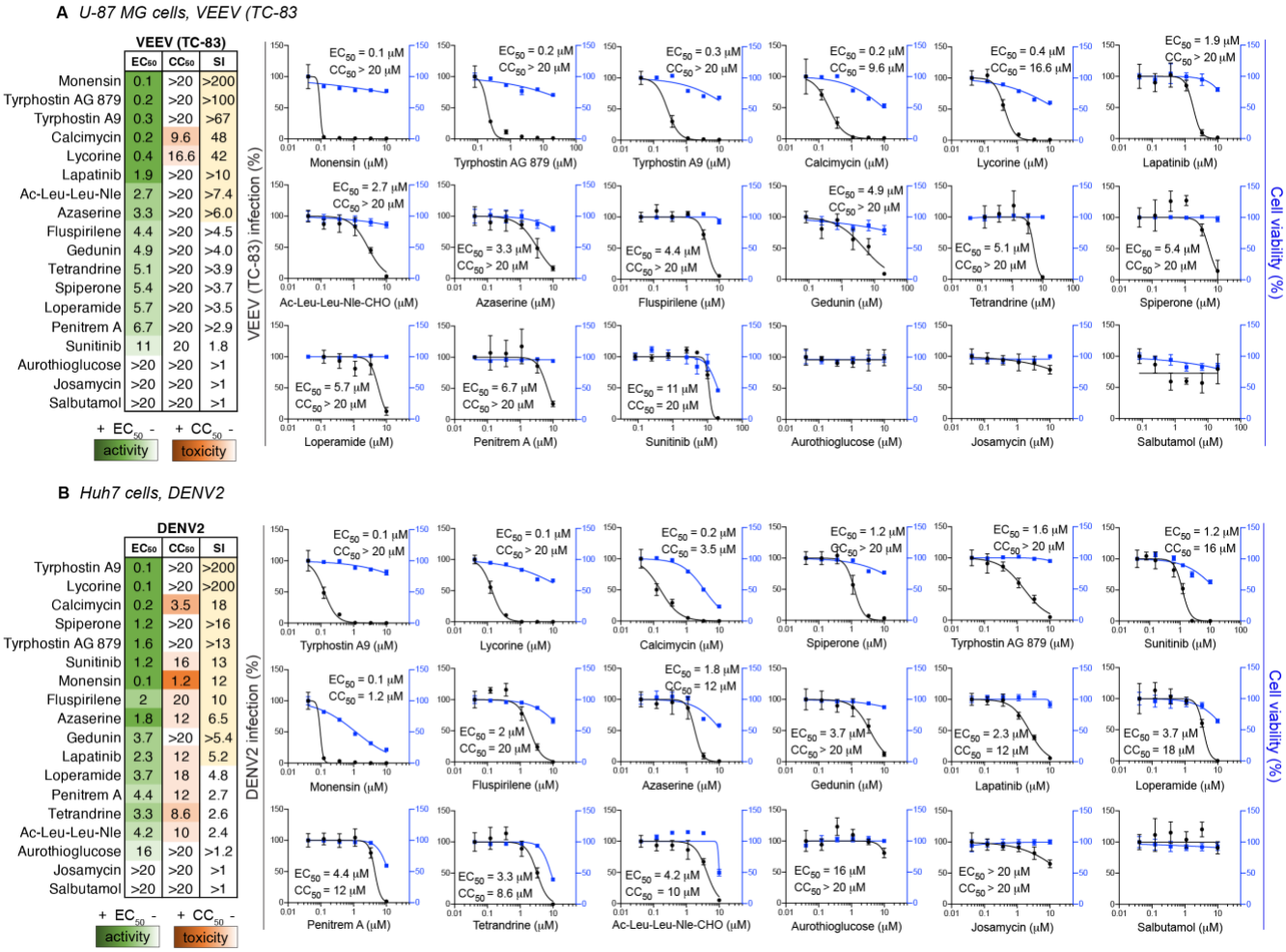

Figure S2. Related to Figure 1.

Broad-spectrum potential of hits and kinase inhibitor set,

(A-D) The 18 compounds emerging from the HTS were tested for their effect on VEEV (TC-83) (A) and DENV2 (B) infections in U-87 MG and Huh7 cells, respectively, via luciferase assays, and for their effect on cell viability via alamarBlue assays.

Left panels: Heat maps of the EC_{50} and CC_{50} values of the indicated compounds color-coded based on the antiviral activity (green) and toxicity t(peach). Selectivity indices (SI) greater than 5 are depicted in yellow.

Right panels: Dose response to the indicated compounds of VEEV (TC-83) (MOI=0.1) or DENV2 (MOI=0.05) infections (black) in U-87 MG and Huh7 cells, respectively, via luciferase assays and cell viability (blue) by alamarBlue assays at 24 hours post-infection.

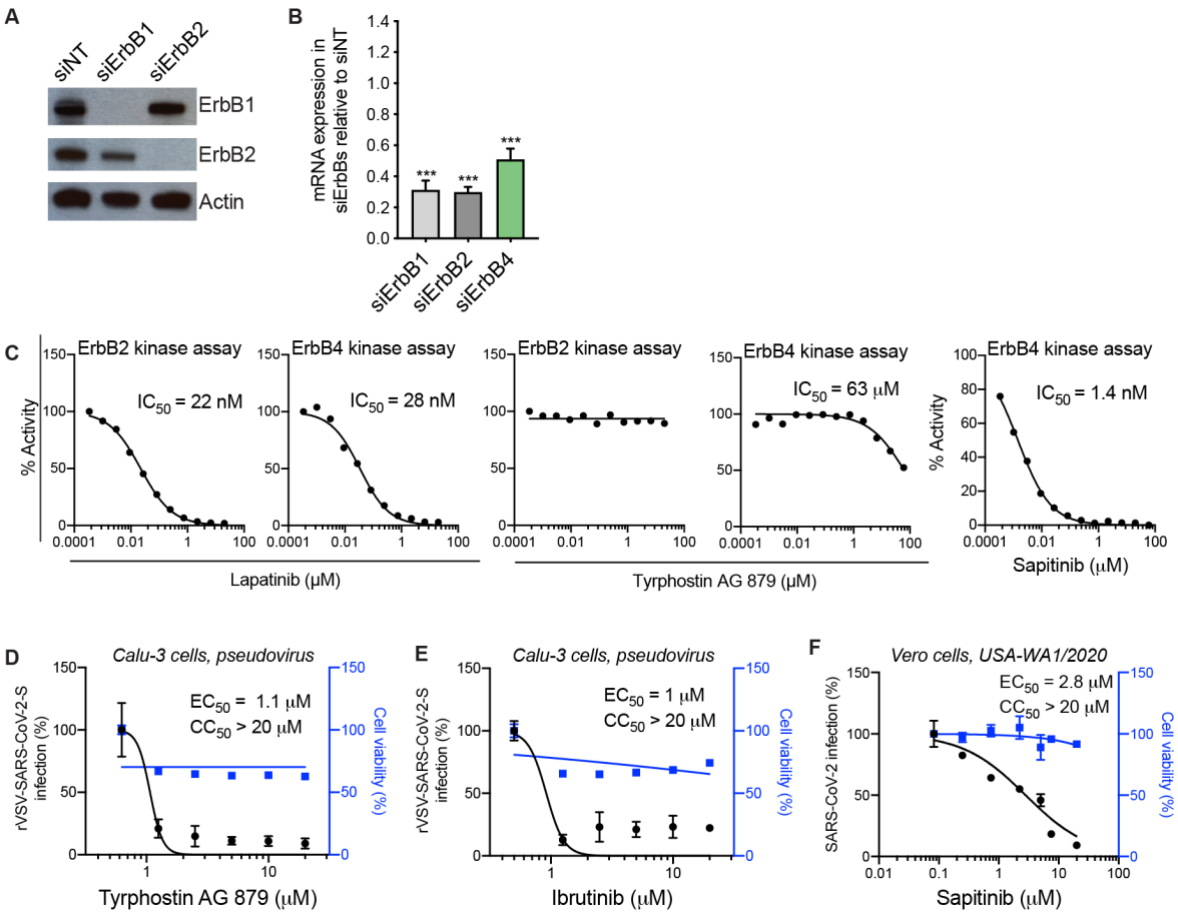

Figure S3. Related to Figure 3.

Validation of ErbB4 as an antiviral target.

(A) Confirmation of siRNA-mediated gene expression knockdown by Western blot in Vero cells at 48 hours after transfection. Notably, two anti-ErbB4 antibodies detected no signal of endogenous protein in Vero cells in two independent experiments.

(B) Confirmation of siRNA-mediated (ON-TARGETplus SMARTpool siRNAs [Dharmacon]) gene expression knockdown by RT-qPCR in Vero cells. Shown is gene expression normalized to GAPDH and expressed relative to the respective gene level in the non-target (siNT) control at 48 hours post-transfection.

(C) Dose response to lapatinib, tyrphostin AG 879 and sapitinib of ErbB2 and/or ErbB4 kinase activity *in vitro* (Nanosyn).

(D, E) Dose response to tyrphostin AG 879 (D) and ibrutinib (E) of rVSV-SARS-CoV-2-S infection (black) by luciferase assays and cell viability (blue) by alamarBlue assays at 24 hours post-infection of Calu-3 cells.

(F) Dose response to sapitinib of SARS-CoV-2 infection (black) by plaque assay and cell viability (blue) by alamarBlue assay 24 hours post-infection of Vero cells.

Data in all panels are representative of 2 or more independent experiments. Individual experiments had 3 biological replicates, means ± SD are shown. **P* < 0.05, ***P* < 0.01**,** ****P* < 0.001 relative to siNT by one-way ANOVA followed by Dunnett's multiple comparisons test.

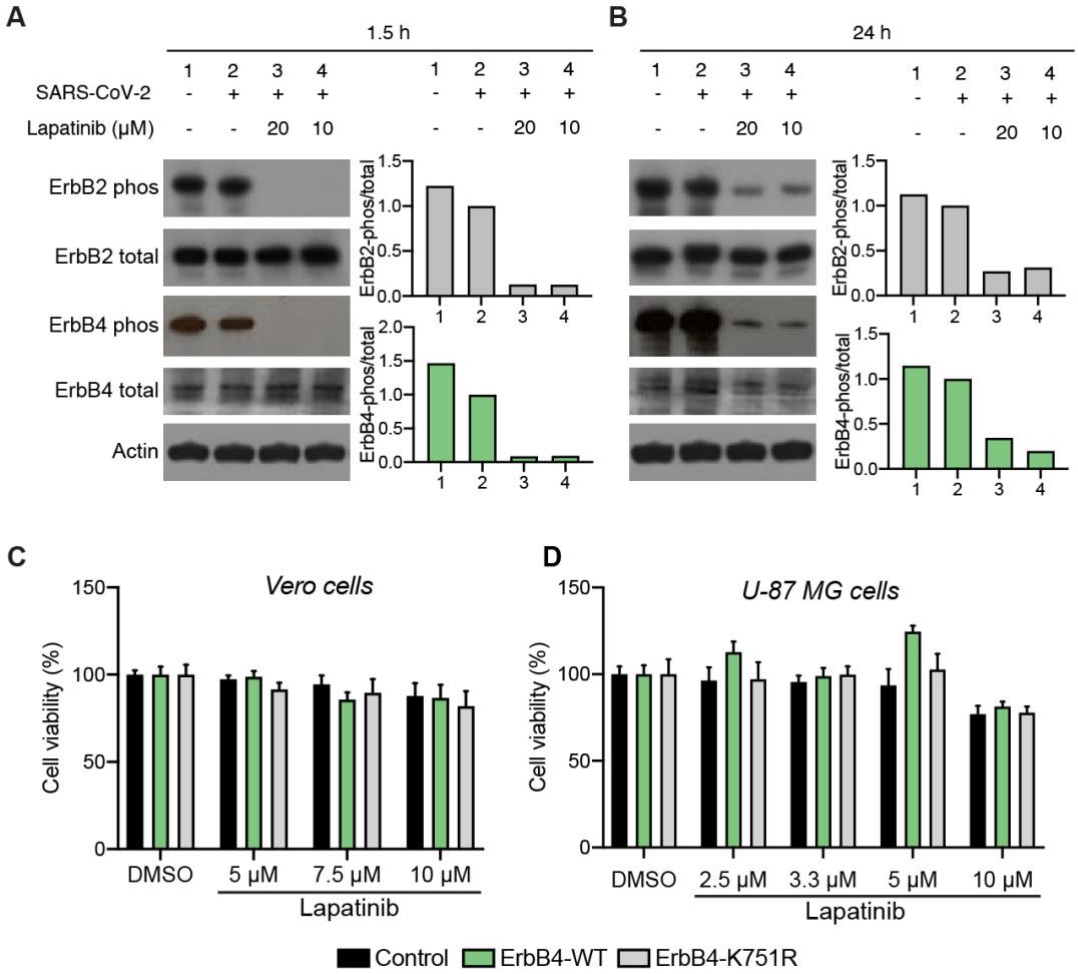

Figure S4. Related to Figure 4.

ErbB4 is modulated by lapatinib and is the molecular target mediating its antiviral effect.

(A, B) ErbB2 and ErbB4 phosphorylation in Calu-3 cells that are uninfected (lane 1), infected and treated with DMSO (lane 2) or infected and treated with lapatinib (lanes 3 and 4) measured by Western blotting 1.5 hours (A) and 24 hours (B) post-infection with SARS-CoV-2 (USA-WA1/2020 strain**,** MOI=1). Shown are representative membranes blotted for phospho- and total ErbB2, ErbB4, and actin and quantitative phospho- to total ErbB ratio data relative to infected cells treated with DMSO (lane 2).

(C, D) Vero (C) and U-87 MG (D) cell viability by alamarBlue assays 48 hours post-transfection of the indicated plasmids. Data relative to the respective DMSO controls are shown.

Data in panels C and D are representative of 2 or more independent experiments. Individual experiments had 3 biological replicates, means ± SD are shown.

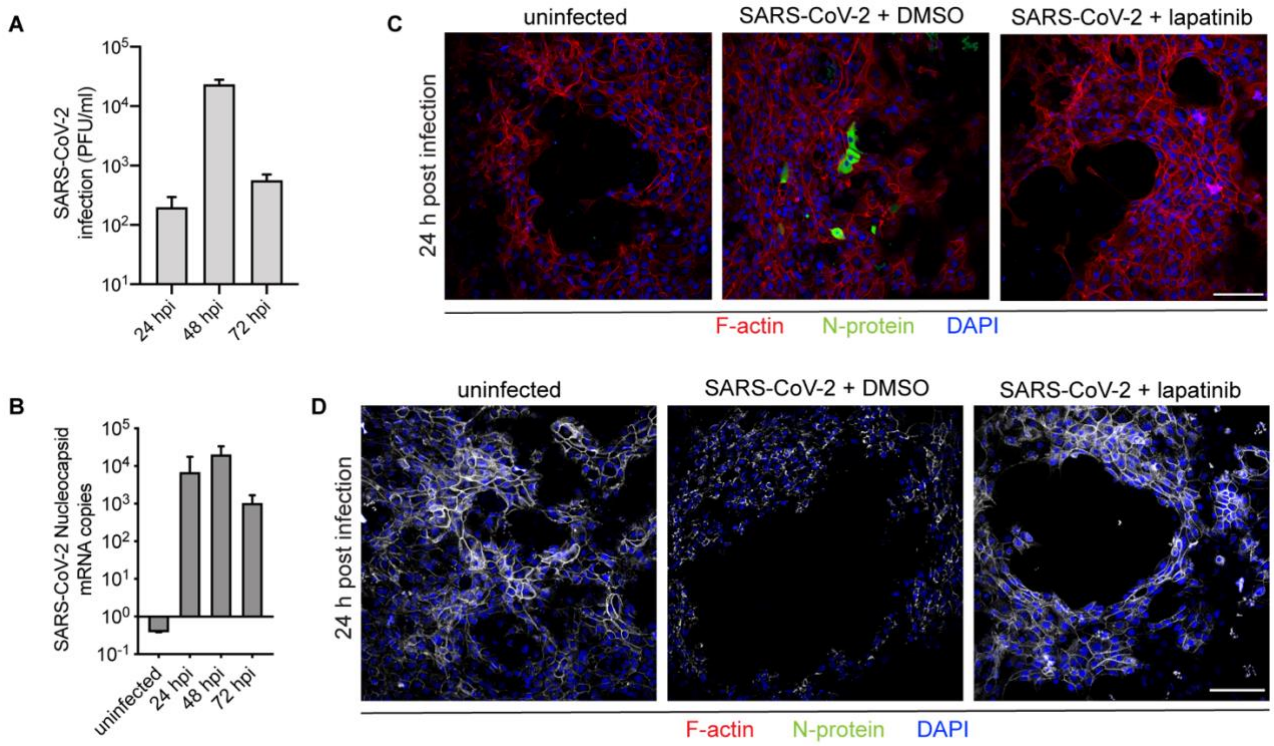

Figure S5. Related to Figure 6.

Human ALOs for studying the antiviral and tissue protective effects of lapatinib.

(A, B) Viral titer by plaque assays in culture supernatants (A) and viral nucleocapsid (N) copy number by RT-qPCR in lysates (B) from human lung organoids at 24, 48 and 72 hours post-infection.

(C) Confocal IF microscopy images of F-actin (red), SARS-CoV-2 nucleocapsid (green) and DAPI (blue) in naïve and SARS-CoV-2-infected ALOs pre-treated with DMSO or 10 µM lapatinib 24 hours post-infection.

(D) Confocal IF microscopy images of Claudin 7 (gray) and DAPI (blue) in naïve or SARS-CoV-2- infected ALOs treated at 4 hours post-infection either with DMSO or 10 µM lapatinib and imaged at 36 hours post-infection.

Representative merged images at 20x magnification are shown in panels C and D. Scale bars are 100 µm.